Article

Cell Chemical Biology

Dependence on the Pyrimidine Biosynthetic Enzyme DHODH Is a Synthetic Lethal Vulnerability in Mutant *KRAS*-Driven Cancers

Graphical Abstract

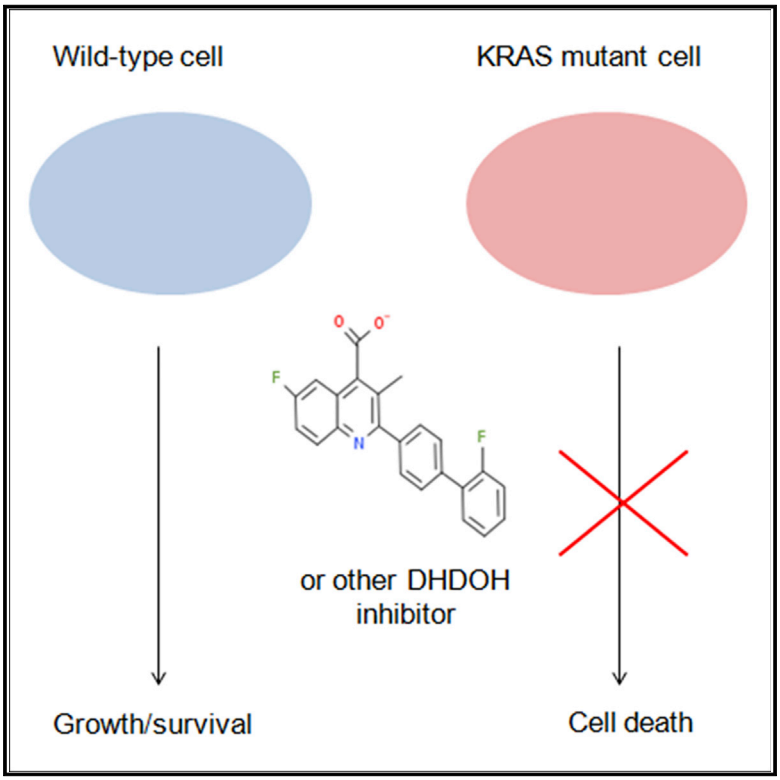

Highlights

- DHODH inhibitors selectively inhibit the growth of *KRAS* mutant cell lines
- The inhibitors affect energy metabolism and glutamine levels in sensitive lines
- DHODH inhibitors synergize with some clinically used anticancer agents

Authors

Malvika Koundinya, Judith Sudhalter, Albane Courjaud, ..., Ivan Cornella-Taracido, Rosalia Arrebola, Aaron Morris

Correspondence

sslicht@gmail.com (S.L.), aaronjmorris@gmail.com (A.M.)

In Brief

Koundinya et al. show that inhibitors of the pyrimidine biosynthetic enzyme dihydroorotate dehydrogenase selectively inhibit the growth of *KRAS* mutant cell lines. Differential sensitivity of the mutant lines correlates with differential effects of the inhibitors on primary energy metabolism and glutamine levels, and the inhibitors synergize with some clinically used anticancer agents.

Koundinya et al., 2018, Cell Chemical Biology *25*, 705–717
June 21, 2018
https://doi.org/10.1016/j.chembiol.2018.03.005

CellPress

Cell Chemical Biology
Article

Dependence on the Pyrimidine Biosynthetic Enzyme DHODH Is a Synthetic Lethal Vulnerability in Mutant *KRAS*-Driven Cancers

Malvika Koundinya,[1] Judith Sudhalter,[1] Albane Courjaud,[2] Bruno Lionne,[2] Gaetan Touyer,[2] Luc Bonnet,[2] Isabelle Menguy,[2] Isabelle Schreiber,[2] Christelle Perrault,[2] Stephanie Vougier,[2] Brigitte Benhamou,[2] Bailin Zhang,[3] Timothy He,[3] Qiang Gao,[3] Patricia Gee,[3] Daniel Simard,[3,4] M. Paola Castaldi,[4] Ronald Tomlinson,[4] Stephan Reiling,[5] Matthieu Barrague,[6] Richard Newcombe,[1] Hui Cao,[7] Yanjun Wang,[8] Fangxian Sun,[8] Joshua Murtie,[8] Mark Munson,[6] Eric Yang,[7] David Harper,[1] Monsif Bouaboula,[1] Jack Pollard,[7] Claudine Grepin,[2] Carlos Garcia-Echeverria,[3] Hong Cheng,[3] Francisco Adrian,[1] Christopher Winter,[1] Stuart Licht,[3,9,*] Ivan Cornella-Taracido,[4] Rosalia Arrebola,[2] and Aaron Morris[1,*]
[1]Cancer Biology, Oncology Division, Sanofi, Cambridge, MA 02138, USA
[2]LGCR-LIT, Sanofi, Vitry-Sur-Seine 94400, France
[3]Biochemistry, Bioanalytics, and Chemical Biology, Oncology Division, Sanofi, Cambridge, MA 02138, USA
[4]Chemistry, Oncology Division, Sanofi, Cambridge, MA 02138, USA
[5]LGCR-SDI, Oncology Division, Sanofi, Cambridge, MA 02138, USA
[6]LGCR, Oncology Division, Sanofi, Cambridge, MA 02138, USA
[7]TEM-BioInformatics, Oncology Division, Sanofi, Cambridge, MA 02138, USA
[8]In Vivo Pharmacology, Oncology Division, Sanofi, Cambridge, MA 02138, USA
[9]Lead Contact
*Correspondence: sslicht@gmail.com (S.L.), aaronjmorris@gmail.com (A.M.)
https://doi.org/10.1016/j.chembiol.2018.03.005

SUMMARY

Activating *KRAS* mutations are major oncogenic drivers in multiple tumor types. Synthetic lethal screens have previously been used to identify targets critical for the survival of *KRAS* mutant cells, but their application to drug discovery has proven challenging, possibly due in part to a failure of monolayer cultures to model tumor biology. Here, we report the results of a high-throughput synthetic lethal screen for small molecules that selectively inhibit the growth of *KRAS* mutant cell lines in soft agar. Chemoproteomic profiling identifies the target of the most *KRAS*-selective chemical series as dihydroorotate dehydrogenase (DHODH). DHODH inhibition is shown to perturb multiple metabolic pathways. *In vivo* preclinical studies demonstrate strong antitumor activity upon DHODH inhibition in a pancreatic tumor xenograft model.

INTRODUCTION

Despite the advance of pathway-targeted therapeutics, *KRAS* mutant cancers still remain a largely unmet medical need. The prevalence of activating *KRAS* mutations is particularly high (greater than 90%) in pancreatic ductal adenocarcinoma (Bardeesy and DePinho, 2002), which has a notoriously poor prognosis. *KRAS* mutations are also prevalent in lung and colon cancers, and the presence of these mutations negatively impacts therapeutic efficacy (Linardou et al., 2008). While direct targeting of the KRAS protein has shown renewed promise (Hunter et al., 2014; Ostrem et al., 2013; Sun et al., 2012), KRAS inhibitors have not yet entered the clinic. Synthetic lethality screens have frequently been used to find alternative points of intervention in mutant *KRAS*-driven cancers, but the results of these screens have not yet been translated to clinical benefit.

Previous synthetic lethal screening efforts (Cox et al., 2014) have mainly used RNAi as a means of identifying potential targets (Barbie et al., 2009; Kim et al., 2016; Luo et al., 2009; Scholl et al., 2009), although a few screens (Shaw et al., 2011; Steckel et al., 2012) have been performed with small chemical libraries. In all cases, these screens have relied on adherent monolayer (2D) cell cultures, and in most cases have used only a matched pair of mutant/wild-type (WT) cell lines. To improve the probability of finding translatable targets, it might be beneficial to use more physiologically relevant cellular models and to screen larger panels of cell lines (Cox et al., 2014).

In an effort to discover translatable mutant *KRAS* synthetic lethal targets, we have performed a 3D clonogenic synthetic lethal screen with a diverse small-molecule library of 280,000 compounds across six mutant *KRAS*-dependent cell lines and four *KRAS*-independent cell lines. We report here the results from this screen, and the identification and characterization of dihydroorotate dehydrogenase (DHODH) as the target of one of the most *KRAS* mutant-selective compounds. As expected, DHODH inhibition prevents *de novo* pyrimidine biosynthesis, which appears to be a particularly important pathway in the growth/survival of *KRAS* mutant cells. DHODH inhibition also substantially decreases cellular levels of glutamine and glutamate, suggesting a connection to the previously established glutamine dependence of *KRAS* mutant cells (Son et al., 2013; Weinberg et al., 2010). We also show that brequinar, a DHODH inhibitor that has previously failed to demonstrate efficacy in clinical trials as an anticancer agent (Moore et al., 1993), exhibits

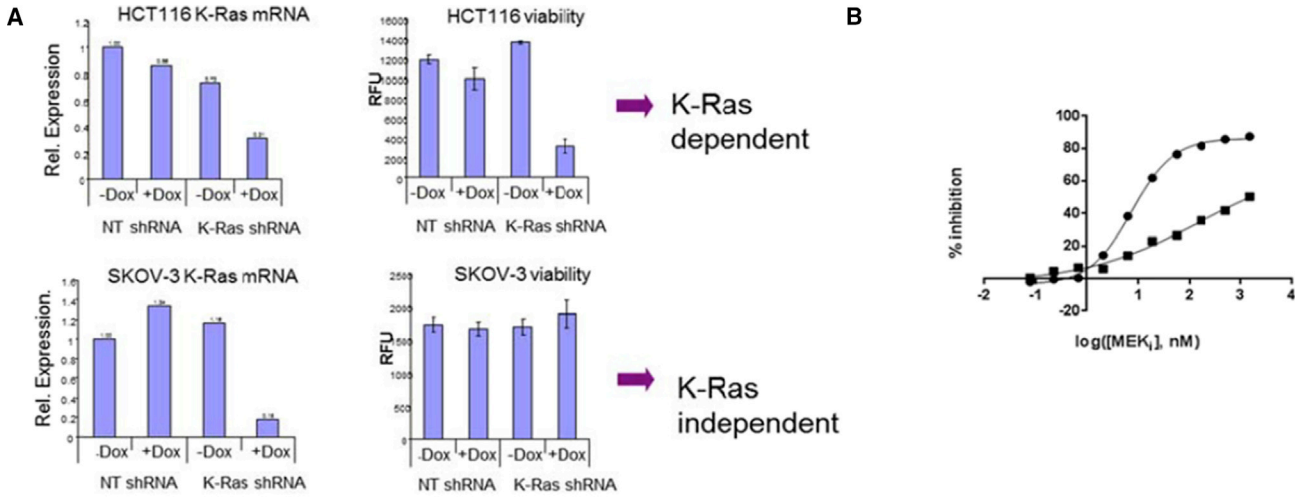

C

Cell line	Tissue	K-Ras	B-Raf	PIK3CA	EGFR	Growth soft agar	K-Ras dependency
PANC-1	Pancreas	G12D htz	wt	wt	wt (4,1 copies)	Yes	Yes
KP-4	Pancreas	G12D htz	wt	wt	wt	Yes	Yes
CFPAC-1	Pancreas	G12V htz	wt	wt	wt	Yes	Yes
MiaPaCa-2	Pancreas	G12C htz	wt	wt	wt	Yes	Yes
HCT116	Colon	G13D htz	wt	H1047R	wt	Yes	Yes
DLD-1	Colon	G13D htz	wt	/	wt	Yes	Yes
SK-OV-3	Ovary	wt	wt	H1047R	wt (1,4 copies)	Yes	No
ACHN	Kidney	wt	wt	wt	wt	Yes	No
H1299*	Lung	wt	wt	wt	wt	Yes	No
UISO-BCA-1	Breast	wt	wt	/	/ (3,4 copies)	Yes	No

* H1299 expresses mutant N-Ras

Figure 1. Determination of *KRAS* Dependence for a Panel of Cell Lines Cultured in 3D

(A) RNAi knockdown of *KRAS* impairs growth and viability of HCT116 (mutant *KRAS*) cells in 3D culture, but SK-OV-3 (*KRAS* WT) cells are not affected. Non-targeted (NT) shRNA was used as a negative control. Dox, doxycycline; RFU, relative fluorescence units.

(B) KP-4 cells (*KRAS* mutant) in 3D culture (circles) are more sensitive to a MEK inhibitor (pimasertib) than the same cells in 2D culture (squares).

(C) Panel of validated mutant *KRAS*-dependent and -independent cell lines.

Error bars represent the standard error of the mean. See also Figures S1 and S2. EGFR, epidermal growth factor receptor.

strong *in vivo* antitumor activity in a *KRAS* mutant pancreatic tumor xenograft model. The links observed *in vitro* between *KRAS* status and a requirement for metabolic flux through the *de novo* pyrimidine biosynthetic pathway suggest new strategies for the clinical application of potent DHODH inhibitors against *KRAS* mutant cancers.

RESULTS

KRAS Dependency of Cell Lines Used for Screening

The panel of cell lines for screening was selected based on the dependence of growth and viability on mutant *KRAS* status. Because of the important contribution of oncogenic KRAS signaling to robust anchorage-independent growth (Campbell et al., 2007; Guerrero et al., 2000), we assessed the *KRAS* dependence of cell lines based on the impact of *KRAS* knockdown in a soft agar clonogenic growth assay. *KRAS* mutant cell lines showing a reduction in growth upon *KRAS* knockdown greater than 50% were designated as *KRAS*-dependent, while *KRAS*-independent cell lines were defined as those in which *KRAS* knockdown had no significant effect (Figure 1A).

In testing growth conditions, we discovered that culturing cells in soft agar (3D culture) had a dramatic effect on their sensitivity to inhibition of Ras-MEK-ERK signaling. Cells cultured in 3D exhibited a half maximal inhibitory concentration (IC_{50}) for the MEK inhibitor pimasertib that was approximately two orders of magnitude less than the same cells cultured on plastic (2D culture) (Figure 1B). Since 3D culture is likely to be a more faithful model for tumors *in vivo*, these conditions were chosen for screening.

An additional important consideration in selecting cell lines was finding *KRAS* WT cell lines with 3D growth capacity and kinetics comparable to *KRAS* mutant cell lines. Based on the criteria of *KRAS* dependence and growth rate, we selected a panel that included six *KRAS*-dependent and four *KRAS*-independent cell lines (Figure 1C). All the *KRAS*-independent cell lines chosen had WT *KRAS* genes. Notably, one cell line (H1299) presented an activating mutation of *NRAS*, which

provided a unique control for the distinct oncogenic impact of mutant KRAS relative to other Ras isoforms.

A Screen for Small Molecules with Selective Cytotoxicity toward *KRAS* Mutant Cell Lines

The chosen cell lines were used in a high-throughput screen of a 280,000-compound chemical library (Figure S1). Following an initial primary screen for effects on viability in five *KRAS* mutant lines, a *KRAS* WT line was added to the panel, and actives were confirmed and tested for *KRAS* mutant selectivity. The list of active compounds was filtered to remove frequent hitters and other compounds known to be problematic in high-throughput screens. Potency of cell growth inhibition (IC_{50}) against the five *KRAS* mutant lines/one *KRAS* WT line was measured for confirmed actives of interest, and compounds were chosen for further analysis based on their selectivity for mutant lines.

To find compounds with high selectivity for *KRAS* mutant lines, potencies and efficacies were plotted (Figure S2). The molecules exhibiting both high potency and high efficacy were selected. The list was further curated by removing promiscuous and/or chemically intractable compounds, leaving a total of 277 compounds. Those were tested against an expanded panel of six *KRAS* mutant and four *KRAS* WT cell lines. Based on their differential activities against mutant and WT lines in this broader panel, the compounds were divided into tiers (Figure S2B).

The compounds exhibiting high potency and *KRAS*-selectivity came from a number of chemical series. As expected, a MEK inhibitor, PD-0325901, was one of the most selective inhibitors of *KRAS* mutant lines. It showed activity against all six *KRAS* mutant lines, but was only active against one WT line. However, the most potent and *KRAS* mutant-selective compounds belonged to another series, based on a thiazolimine scaffold. Active members of this series were chosen for characterization in a second screen against a large cancer cell line panel.

Because of the difficulty of screening a larger cell line panel in the 3D format (the automated work stream used for large-scale screening was customized for 2D cultures and many WT lines failed to grow robustly in 3D culture), only the thiazolimine series was tested against this panel of lines (374 diverse cancer cell lines characterized with respect to genetic mutations, copy number variations, and mRNA expression levels) in 2D culture. An analysis of the results (Figure 2A) showed that the thiazolimines were among the most *KRAS* mutant-selective agents tested; the *KRAS* mutant lines in the panel were, on average, more sensitive to the thiazolimines, and this selectivity was comparable to that observed for the MEK inhibitor pimasertib. In a complementary analysis, the known mutations in the cell line panel were examined to determine which were most highly enriched among cell lines that responded to the thiazolimine compound **1** (Table S1). This analysis showed that *KRAS* was the gene in which mutations were most strongly associated with sensitivity to the compound (Figure 2B). In addition, many lung and pancreatic cell lines in the panel were sensitive to compound **1**, while cell lines from tissues of origin where *KRAS* mutation is less prevalent tended to be less sensitive to it (Figure 2C), consistent with a substantial effect of the *KRAS* mutation on differential sensitivity. These data thus suggest that the thiazolimines inhibit a pathway required for survival of *KRAS* mutant cell lines.

Chemoproteomic Discovery of Potential Targets of the Thiazolimine Series

Based on the promising results from the synthetic lethal screen and the cell line profiling, the thiazolimine series was chosen for compound deorphaning via a chemoproteomics approach. For this chemoproteomics approach, it was judged likely that, for cells that exhibited thiazolimine sensitivity in both 2D and 3D culture, the specific molecular target of the thiazolimine series would be the same in both culture systems, although the details of the phenotypic consequences of target inhibition might differ. In order to build a solid-supported affinity reagent for use in protein target pull-downs, the lead thiazolimine was functionalized with a short amine-terminated linker at various positions. Compound **14**, in which a phenol group was O-alkylated with the linker, retained activity in DLD-1 and KP-4 cells, thus validating the phenol moiety as a suitable attachment point for the solid support. Based on these results, an affinity reagent (compound **18**), in which **14** was attached to Sepharose beads, was prepared.

A SILAC-based (Mann, 2006) strategy was used to identify proteins that bind specifically to the thiazolimine-derivatized solid support (Figure 3A). To provide labeled proteome samples for affinity pull-downs, KP-4 cells were grown in either 2D or 3D cell culture using media containing amino acids with either a light or heavy stable isotope label. In the first of three related experiments, SILAC pull-downs were performed at two concentrations of the active competitor compound **2** (1× or 20× its half maximal effective concentration [EC_{50}]; Table S1), comparing the pull-down efficiency in the presence of the competitor to the efficiency in the presence of DMSO as a control (Figure 3B). Dihydroorotate dehydrogenase (DHODH; Uniprot ID PYRD) was among the proteins most highly differentially competed from the affinity matrix. DHODH was identified from multiple peptides in the SILAC experiments. The SILAC ratios observed were qualitatively dependent on the concentration of competitor compound **2**. These observations are consistent with a specific interaction between DHODH and the affinity reagent-derivatized support.

In a second experiment, a four-plex tandem mass tag pull-down experiment on 2D-cultured KP-4 cells was used to quantify the dose-response trend observed in the SILAC experiment. The decrease in DHODH affinity pull-down correlated well with the concentration of free competitor compound **2** (Figure 3C). That observation further supports the hypothesis that DHODH binds specifically to the derivatized solid support.

A third experiment was designed to determine whether DHODH would also exhibit affinity for a biologically inactive homolog of the active thiazolimine compound **2**. Both the active compound **2** and its close analog **3** (Table S1), which does not inhibit KP-4 cell growth, were used as competitors in a SILAC experiment. The results of this experiment (Figure 3D) show that DHODH was selectively competed off the affinity matrix by **2** relative to **3**. This observation suggests that within the thiazolimine series, bioactivity against KP-4 cells is associated with binding affinity for DHODH. It is consistent with the hypothesis that the thiazolimine series exerts its effect on cell growth by inhibiting DHODH.

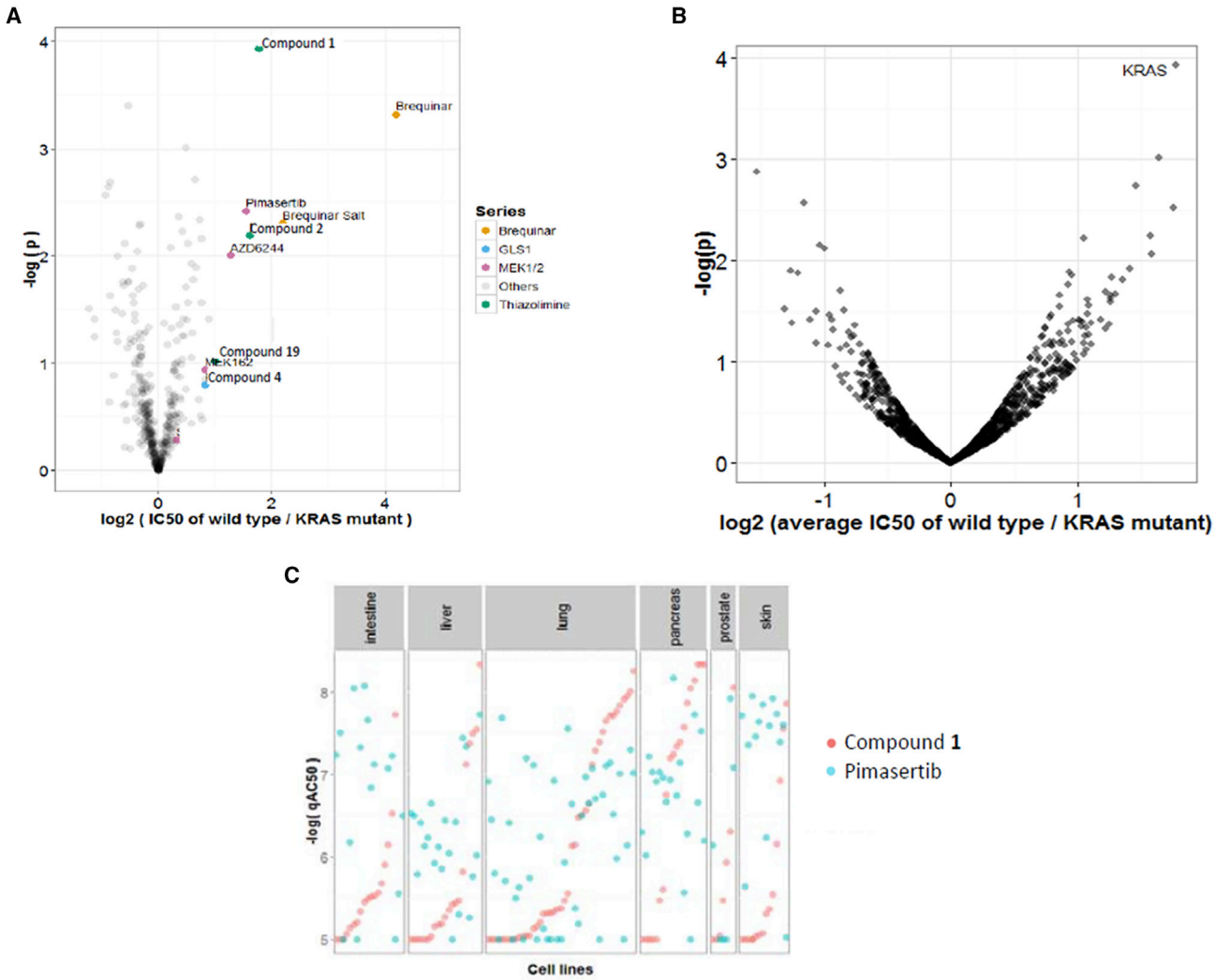

Figure 2. Phenotypic Profiling of Chemical Hit Series across a Large Cancer Cell Line Panel Identifies One Hit Series as Highly Selective for *KRAS* Mutant Cell Lines

(A) Compounds from the thiazolimine series are among the most selective for *KRAS* mutant cell lines. Statistical significance is plotted as a function of selectivity, as expressed as the ratio of average potency against *KRAS* WT/*KRAS* mutant lines.

(B) *KRAS* mutation status is the best predictor of cell sensitivity to the thiazolimine series among the mutations represented. Statistical significance is plotted against mutant/WT differential sensitivity to thiazolimine compound **1**.

(C) Compound **1** (red symbols) is highly potent against many pancreatic and lung cancer cell lines. Pimasertib (blue symbols) is plotted for comparison.

Mechanistic Validation of the DHODH Target Hypothesis

To determine whether binding of the thiazolimines inhibits DHODH's enzymatic activity, we investigated the inhibitory potency of a number of thiazolimines against purified recombinant DHODH. The tested compounds were highly potent on average (a median IC_{50} of 11 nM), with the more potent members of the series being comparably potent to brequinar, a previously characterized DHODH inhibitor with an IC_{50} of 5–10 nM (Chen et al., 1992; McLean et al., 2001). These results indicate that the thiazolimines bind to DHODH in a mode that prevents enzymatic catalysis.

We next investigated whether the compounds' DHODH inhibitory potencies were correlated with their potencies for cell growth inhibition (Figure 4A). Here, the issue of biological differences between 2D and 3D cultures becomes relevant; however, by choosing cells that exhibit a growth/survival phenotype in 2D culture, we can correlate DHODH inhibition with cellular phenotype in a 2D system where the phenotype is similar to what is observed in 3D cultures. A correlation analysis reveals a Spearman's coefficient of 0.76 between these two potencies ($p = 1 \times 10^{-3}$), consistent with the hypothesis that DHODH inhibition is a key driver of cellular potency. However, there is a substantial (~100-fold) shift toward lower potency when comparing the biochemical with the cellular assay (e.g., compounds with ~10 nM IC_{50} values in the biochemical assay exhibit IC_{50} values of ~1 μM in the cellular assay).

As an additional and more direct test of whether the thiazolimines also potently inhibit DHODH in a cellular context, a

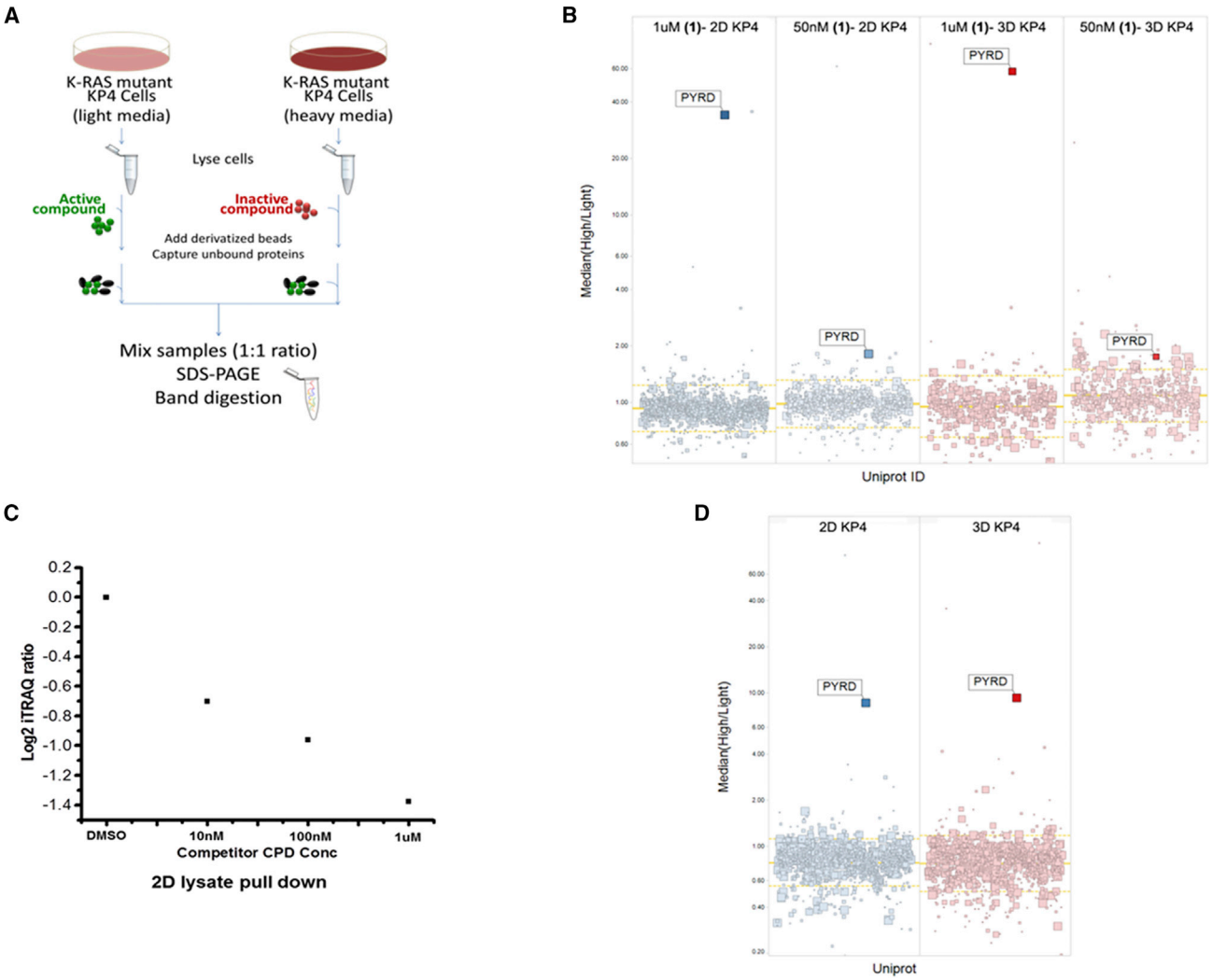

Figure 3. Chemoproteomic Deorphaning of the Thiazolimine Series Identifies DHODH (PYRD) as a Candidate Target for the Series

(A) Outline of SILAC experiments in which light/heavy isotopically labeled media encodes the presence of active/inactive compound (or vehicle).

(B) SILAC experiments in which active compound (compound **2**) is used as a competitor at two concentrations (1× EC_{50} or 20× EC_{50}). KP-4 cells were cultured in 2D (blue graphs, left-hand side) or 3D (red graphs, right-hand side).

(C) Quantitative dose-response relationship for a soluble competitor compound by iTRAQ.

(D) SILAC experiment to determine ratio of proteins competed by active (compound **2**)/inactive (compound **3**) free compound. Lysates from 2D cultures (blue graph, left-hand side) or 3D cultures (red graph, right-hand side) were used.

See also Table S1.

mass spectrometry-based pharmacodynamic (PD) assay for dihydroorotate (DHO) was used to measure the accumulation of this DHODH substrate in cells. The results (Figure 4B) show that the thiazolimines' potencies for cellular inhibition of DHODH activity are highly correlated with their potencies for inhibition of cell growth (Spearman's coefficient of 0.96, $p = 3 \times 10^{-3}$). These data thus support the hypothesis that thiazolimines inhibit cell growth in *KRAS* mutant cells by inhibiting DHODH enzymatic activity. Biochemical and cellular potencies are also reasonably well-correlated for DHODH inhibitors from other chemotypes (e.g., brequinar and analogs) (Figure S3A).

Dose-response relationships were measured in all three assays (biochemical, cell PD, and cell viability) for representative molecules in each series. The data (Figures 4C and S3B) indicate that for all DHODH inhibitors examined, potencies in the three assays are mutually correlated with each other (Spearman coefficients of 0.7, 0.8, and 0.96 for biochemical/PD, biochemical/phenotypic, and PD/phenotypic correlations, respectively). Thus, on-target effects of DHODH enzyme inhibitors appear to contribute to growth inhibition of *KRAS* mutant cells.

The hypothesis that the thiazolimines act via DHODH inhibition suggests that supplementation with exogenous pyrimidines may rescue cell growth inhibition. Treatment of cells with exogenous uridine, which can complement deficits in *de novo* pyrimidine biosynthesis (Connolly and Duley, 1999), was used to test this prediction. As predicted, addition of uridine rescued cell growth in thiazolimine-treated cells (Figure 4D). A similar rescue effect was observed for cells treated with brequinar (Figure S4).

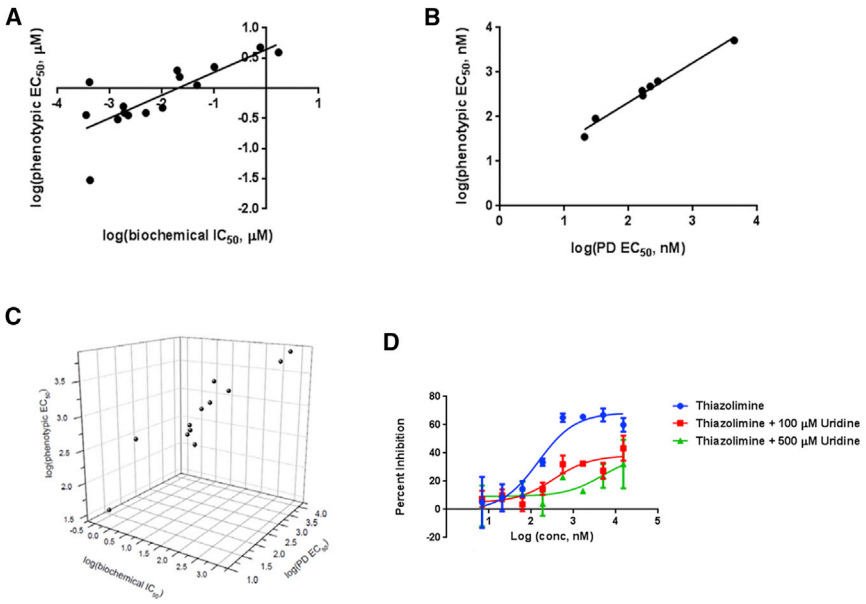

Figure 4. Validation of DHODH as a Biologically Relevant Target for the Thiazolimine Series in a *KRAS* Mutant Cell Line

(A) Correlation of IC_{50} in the biochemical assay with EC_{50} in the cell growth inhibition assay (values expressed as the logarithm).

(B) Correlation of EC_{50} in the pharmacodynamic (PD) assay with EC_{50} in the cell growth inhibition assay.

(C) Correlation of biochemical IC_{50}, PD EC_{50}, and cell growth inhibition EC_{50}.

(D) Dose-dependent rescue of compound **2**-induced cell growth inhibition by uridine. Blue symbols: thiazolimine dose-response in the absence of uridine. Red symbols: 100 μM uridine. Green symbols, 500 μM uridine.

Error bars represent the standard error of the mean. See also Figures S3 and S4.

Notably, the concentration of uridine required for complete rescue (>100 μM) is greatly in excess of the normal physiological serum concentration (~5 μM; Connolly and Duley, 1999).

Mitochondrial Metabolic Effects and Other Cellular Consequences of DHODH Inhibition

In addition to the role of DHODH in *de novo* pyrimidine biosynthesis, its role in mitochondrial electron transport may also contribute to these inhibitors' effects.

To investigate whether DHODH inhibitors affect the mitochondrial membrane potential, we measured mitochondrial potential in KP-4 cells as a function of DHODH inhibitor dose (Figure 5A). The results show that DHODH inhibitors from two distinct chemical series potently and dose-dependently induce mitochondrial depolarization. The MEK inhibitor pimasertib, which also inhibits KP-4 cell growth, does not affect mitochondrial membrane potential. In addition to the inactive compound **3,** teriflunomide, which is a much less potent DHODH inhibitor than brequinar (Davis et al., 1996; Erra et al., 2011; McLean et al., 2001) or the best thiazolimine compounds, also has a minimal effect on mitochondrial membrane potential (data not shown). These results suggest that mitochondrial depolarization may contribute to the effects of potent DHODH inhibitors in cells.

Inhibition of DHODH might also affect steady-state metabolite levels, since glutamine is a starting metabolite for *de novo* pyrimidine biosynthesis and DHODH is also linked to the citric acid cycle via its role in mitochondrial electron transport. For these detailed metabolomics experiments and subsequent *in vivo* experiments, we chose to use brequinar rather than a thiazolimine compound due to the extensive previous preclinical and clinical characterization of brequinar as a DHODH inhibitor. Mass spectrometric analysis indicates that treatment with brequinar perturbs the levels of a number of metabolites (Figures 5B and S5). In KP-4 cells at the 24-hr time point after drug treatment, the effects include increases in the levels of malate, fumarate, and aspartate, and decreases in the levels of glutamate, succinate, and αKG. Brequinar also induces a substantial dose-dependent decrease in the steady-state level of glutamine (Figure 5B); a comparable but more potent decrease is observed using compound **2**.

To further investigate how DHODH inhibition might differentially affect *KRAS* WT and mutant cells, we carried out metabolomics experiments to compare the effects of brequinar on *KRAS* WT and mutant DLD-1 cells, as well as to compare metabolite levels between the WT and mutant cells in the absence of drug (Figures S6 and S7). Consistent with results in other cell lines, the mutant DLD-1 cells exhibited a greater response to brequinar and compound **2** than otherwise isogenic cells containing the WT allele (Figure S6). In the *KRAS* mutant DLD-1 cells at the 4-hr time point after drug treatment (i.e., before effects on cell viability are observed), the effects include an increase in the steady-state concentrations of fructose 1,6-bisphosphate; this increase is not observed in the WT cell line (Figure S7). In addition, the flux of glutamate (as judged by the change in isotopic incorporation from ^{13}C-glutamine) increases in response to brequinar treatment, both for *KRAS* mutant and *KRAS* WT cells. In *KRAS* mutant cells, brequinar treatment is also associated with a large increase in AMP and ADP concentrations and a concomitant decrease in the concentration of ATP, indicative of energy stress. In contrast, brequinar treatment of *KRAS* WT cells leads to at most a modest increase in AMP and ADP, with an increase in ATP observed as well, suggesting that the mutant cells are differentially sensitive to energy stress induced by DHODH inhibition. DHODH inhibition does not affect the ratio of reduced/oxidized glutathione at the 4-hr time point, but, consistent with previous studies (Yun et al., 2015), the reduced/oxidized glutathione ratio is markedly smaller in *KRAS* mutant than *KRAS* WT cells.

In addition to perturbing metabolite levels, DHODH inhibition also induces cell-cycle arrest. Flow cytometric analysis of cellular DNA content after treatment of KP-4 cells with compound **2** (Figures 5C and S8) indicates that the cells become arrested in S phase. Inhibition of pyrimidine metabolism and/or other metabolic perturbations may mediate this cell-cycle arrest.

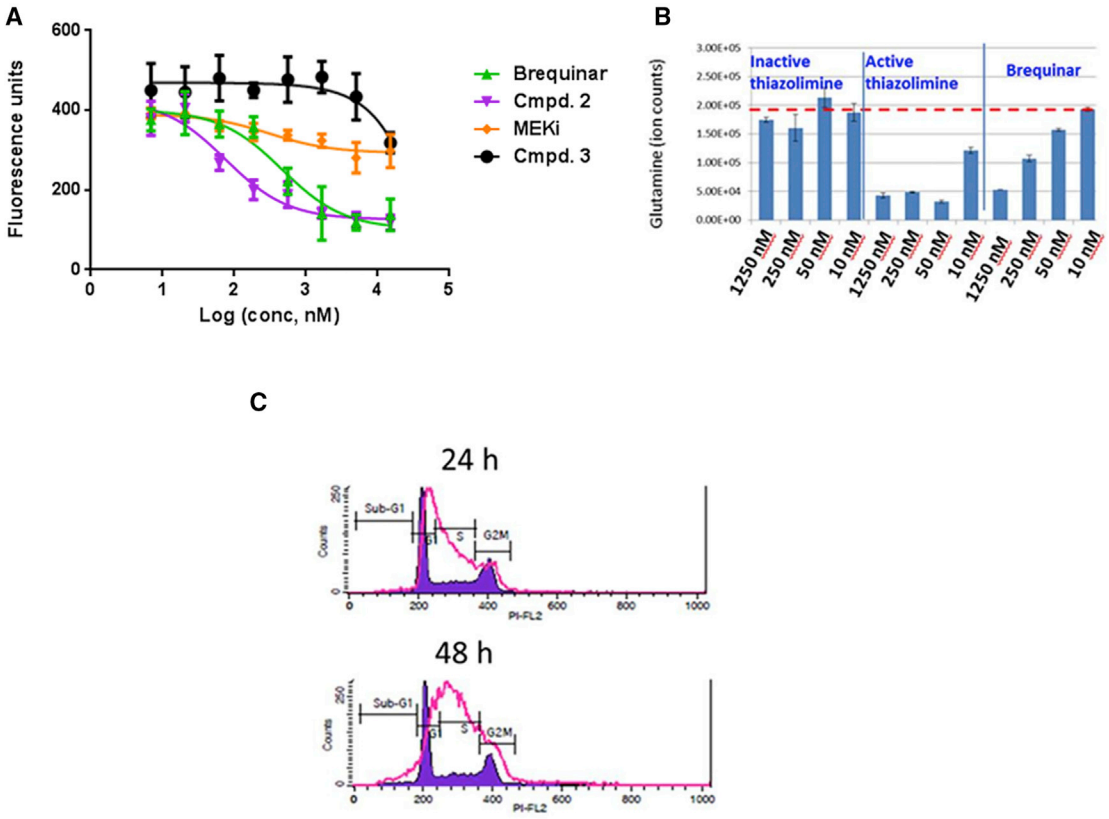

Figure 5. Effects of DHODH Inhibition on Cellular Metabolism and the Cell Cycle

(A) Potent DHODH inhibitors induce mitochondrial depolarization in KP-4 cells. Magenta symbols: compound **2**; green symbols, brequinar; orange symbols, pimasertib; black symbols, inactive thiazolimine (compound **3**).

(B) DHODH inhibitors (inactive thiazolimine **3**, active thiazolimine **2**, and brequinar) decrease cellular levels of glutamine.

(C) Treatment of KP-4 cells with thiazolimine compound **2** for 24–48 hr induces arrest in S phase. DNA content was quantified using propidium iodide. Pink histogram: cells treated with compound **2**. Blue histogram: DMSO-treated cells.

Error bars represent the standard error of the mean. See also Figures S5–S8.

In Vivo Antitumor Activity of a DHODH Inhibitor

Although DHODH inhibition has well-defined effects on cancer cells *in vitro*, the potential availability of metabolites from other tissues *in vivo* might limit the applicability of the *in vitro* findings. To address this issue, we carried out *in vivo* studies of the effects of brequinar on xenografts of KP-4 cells. Measurements of metabolite concentration in the tumors (Figure 6A) establish that the DHODH substrate dihydroorotate (DHO) in the tumor builds up following accumulation of brequinar, consistent with *in vivo* target engagement. Similarly, measurement of the pyrimidine biosynthesis product uridine as an additional PD marker (Figure 6B) indicates that it becomes depleted. In addition, as observed *in vitro*, glutamine was depleted in the tumor after brequinar treatment (Figure 6C).

In addition to demonstrating target engagement, the xenograft studies also indicate that brequinar suppresses tumor growth *in vivo* in a dose-dependent fashion (Figure 6D). Consistent with previous reports (Moore et al., 1993; Peters et al., 1990, 1992), brequinar also exhibits dose-dependent toxicity as measured by body weight loss in treated mice (Figure 6E); at the 30 mg/kg dose, this body weight loss was large enough to require termination of that arm of the study. However, at the 3 mg/kg and 10 mg/kg doses that supported substantial tumor growth inhibition, body weight loss was minimal (at 3 mg/kg) or transient (at 10 mg/kg) over the course of the study, defining a therapeutic window for dosing in this system.

Synergistic Combinations of a DHODH Inhibitor with Other Drugs

Because DHODH inhibitors have already been clinically tested without demonstrating efficacy (Moore et al., 1993; Peters et al., 1992), we investigated whether brequinar (the DHODH inhibitor for which the most clinical data is available) might exhibit greater efficacy *in vitro* in combination with another drug. A set of 23 potential enhancer compounds with known mechanisms of action was chosen based on previous screening results against *KRAS* mutant cells and on an assessment of whether the compounds' mechanisms of action were likely to synergize with DHODH inhibition. These compounds were screened against KP-4 cells in a 12 × 12 dose matrix with brequinar (in 2D culture) to test for synergistic response.

The combination screen identified a number of drugs that synergize with brequinar *in vitro* (Figures 7A and 7B) using at least

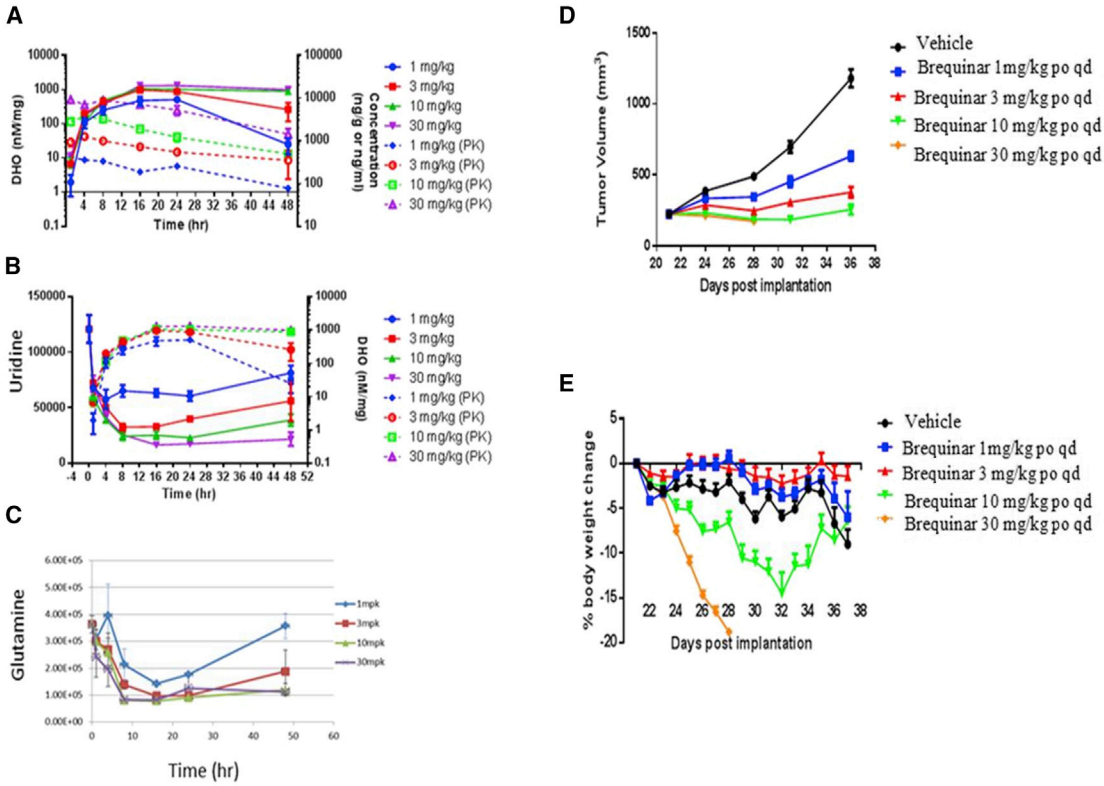

Figure 6. Brequinar Exhibits an Antitumor Effect *In Vivo* Against KP-4 Xenograft Tumors

(A) Accumulation of DHODH substrate DHO in tumors is correlated with the concentration of brequinar in the tumor.

(B) Accumulation of DHO is correlated with depletion of uridine *in vivo*. Uridine concentration is presented in a.u. corresponding to ion counts from mass spectrometry.

(C) Depletion of tumor glutamine is associated with brequinar treatment and occurs with a time course similar to uridine depletion.

(D) Brequinar suppresses the growth of KP-4 xenografts. Po, by mouth; qd, every day.

(E) Brequinar exhibits a therapeutic window in the KP-4 xenograft model.

Error bars represent the standard error of the mean.

one standard criterion (Loewe [Chou and Talalay, 1984] and/or HSA [Berenbaum, 1989] drug synergy scores; none of the drugs listed scored as synergistic using the Bliss synergy score [Bliss, 1939]). Notably, two of these (floxuridine, gemcitabine) act directly on enzymes involved in pyrimidine nucleotide biosynthesis, and a third (everolimus) is expected to affect pyrimidine biosynthesis indirectly (Ben-Sahra et al., 2013; Robitaille et al., 2013).

Because glutamate is a product of *de novo* pyrimidine biosynthesis, inhibiting pyrimidine biosynthesis may affect the steady-state glutamate concentration. Experimentally, brequinar as a single agent induces a decrease in steady-state glutamate concentration that, surprisingly, is comparable to the effect of an inhibitor of GLS1, a major contributor to glutamate flux in many cancer cells (Figure 7C). The combination of a GLS1 inhibitor, compound **4** (Table S1) (Gross et al., 2014), with brequinar was observed to decrease glutamate in KP-4 cells to lower levels than observed for equivalent concentrations of either agent individually (Figure 7C); however, it is not yet known whether this effect is due to additivity or synergism between the two agents. No synergistic effect on cell growth was observed for **4**; however, preliminary results indicate that a second-generation GLS1 inhibitor exhibits strong synergy with brequinar (data not shown).

DISCUSSION

The current study integrates results from both a new screen in 3D culture and more conventional screens in 2D culture. Screening in 3D culture has the advantage of sensitizing *KRAS* mutant cells to Raf-MEK-ERK pathway inhibition (Figure 1D), so that the phenotypes observed may be more directly translatable to *in vivo* systems. Empirically, primary screening in 3D culture enabled the discovery of *KRAS* synthetic lethal mechanisms that had not previously been reported. However, screening in large numbers of different cell lines proved to be more technically tractable for 2D cell cultures. While results from both kinds of screens were broadly consistent with each other, responses of 2D-cultured lines to synthetic lethal perturbation varied widely (see, e.g., Figure 2A). These results suggest that 3D culture systems are useful for studying *KRAS* mutant phenotypes, and that results from small numbers of cell lines cultured in 2D may or may not be predictive of results from 3D cultures and/or *in vivo* biology.

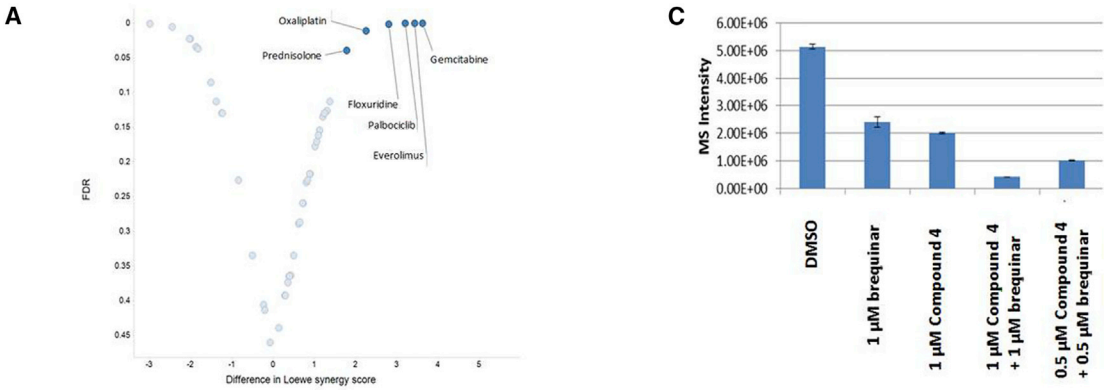

B

Enhancer	Cpd MoA	Loewe	HSAscore
Prednisolone	Glucocorticoid receptor agonist	Yes	
Palbociclib	CDK4 inhibitor	Yes	Yes
Floxuridine	Pyrimidine metabolism	Yes	
Everolimus	mTOR1/2 inhibitor	Yes	Yes
Oxaliplatin	DNA-damaging agent	Yes	
Gemcitabine	DNA metabolism	Yes	Yes

Figure 7. Screening for Agents That Synergize with a DHODH Inhibitor

(A) Plot of statistical significance (adjusted false discovery rate, FDR) versus HSA synergy score.

(B) Compounds exhibiting significant synergy as judged by two different synergy scores (Loewe and HSA). mTOR, mammalian target of rapamycin.

(C) The combination of brequinar sodium and a GLS1 inhibitor (compound **4**) decreases steady-state levels of glutamate in KP-4 cells to a greater extent than either compound alone. Glutamate is quantified as intensity of MS signal (ion counts). Error bars represent the standard error of the mean.

The primary finding of the current work is that *KRAS* mutant cells exhibit a synthetic lethal sensitivity to inhibitors of DHODH. However, it is clear that inhibition of DHODH has pleiotropic effects in cancer cells. Multiple downstream consequences of DHODH inhibition may thus contribute to the selective effect of DHODH inhibitors.

Results in cells and *in vivo* (Figures 5, 6A, and 6B) indicate that, as expected, DHODH inhibition leads to decreased flux through the *de novo* pyrimidine biosynthetic pathway. In addition, cell growth inhibition by DHODH inhibitors is rescued by uridine (Figure 4D), suggesting that inhibition of *de novo* pyrimidine biosynthesis contributes to cytotoxicity. The latter observation further suggests that *de novo* pyrimidine biosynthesis is required for growth and survival in *KRAS* mutant cells.

Previous studies have also linked Ras-Raf-MEK-ERK signaling with increased *de novo* pyrimidine biosynthesis. Decreased expression of an inducible mutant *KRAS* downregulates pyrimidine biosynthetic genes at the transcriptional level (Ying et al., 2012). In addition, MAPK signaling abolishes feedback inhibition of carbamoyl phosphate synthetase, which catalyzes the rate-limiting step in *de novo* pyrimidine biosynthesis (Graves et al., 2000). Notably, glutamine deprivation in *KRAS*-driven cancer cell lines has recently been shown to interfere with deoxynucleotide biosynthesis, leading to S-phase arrest and replicative stress (Patel et al., 2016). Deprivation of pyrimidine nucleotides is thus likely to be a major contributor to the differential effect of DHODH inhibitors on cell viability in *KRAS* mutant cell lines.

Mitochondrial depolarization induced by DHODH inhibition (Figure 5A) may also contribute to the selective effects of DHODH inhibitors on *KRAS* mutant cells. If so, the effect may arise more from pro-apoptotic effects of mitochondrial depolarization (Lemasters et al., 1998) than from impaired oxidative phosphorylation. Oncogenic *KRAS* mutations have been associated with decreased, rather than increased, oxidative phosphorylation: expression of mutant KRAS leads to an increased dependence on anabolic glucose metabolism (Weinberg et al., 2010; Ying et al., 2012), while ablation of mutant *KRAS* leads to an increased dependence on oxidative phosphorylation (Viale et al., 2014). However, to the extent that *KRAS* mutant cells exhibit enhanced flux through *de novo* pyrimidine biosynthesis, they may also exhibit a greater dependence on electron transport through DHODH to maintain consistently hyperpolarized mitochondrial membrane potentials and a pro-survival phenotype. A precedent for an association between hyperpolarized mitochondrial potentials and a pro-survival phenotype can be found in the example of $CD8^+$ memory T cells, for which surplus capacity for oxidative phosphorylation enhances cellular survival (van der Windt et al., 2012).

Measurements of metabolite levels in the current study are also consistent with the idea that *KRAS* mutant cells are differentially dependent on mitochondrial electron transport via DHODH, which may contribute to differential effects of DHODH inhibition. In *KRAS* mutant cells, brequinar treatment is associated with energy stress (Figure S7). However, brequinar does not induce similar energy stress in WT cells. Taken together, these data support the hypothesis that *KRAS* mutant cells are differentially dependent on flux through DHODH for survival, due in part to its role in primary energy metabolism. One possibility is that in *KRAS* mutant cells, increased electron transport via DHODH partially compensates for decreased electron transport via aerobic glucose metabolism.

In addition to a role for DHODH inhibition in primary energy metabolism, the observation of decreased steady-state levels of glutamine and glutamate and increased isotopic exchange into glutamate (a proxy for metabolic flux) upon treatment with a DHODH inhibitor (Figures 5C, 6C, 7G, S5, and S7) suggests a link between DHODH activity and glutamine metabolism, which was previously demonstrated to be crucial for the growth and survival of *KRAS* mutant cancer cells (Son et al., 2013; Weinberg et al., 2010). These observations, as well as the increased steady-state level of aspartate observed upon DHODH inhibition, are consistent with increased conversion of glutamine and oxaloacetate to αKG and aspartate via GOT1. Therefore, the decreased steady-state levels of glutamine appear not to be caused by a lack of available glutamine as a metabolic substrate, but rather by increased consumption of glutamine.

Since the decrease in glutamine levels appears to be associated with increased glutaminolysis rather than a decreased ability to accumulate glutamine, it might be hypothesized that this decrease in glutamine levels does not contribute to impaired growth and survival in *KRAS* mutant cells. However, the observation that uridine rescues both the effect of brequinar on glutamate flux and its cellular phenotypic effect suggests that the metabolic effects of DHODH do contribute to its broader biological effects. In addition, the results are consistent with synergism between GLS1 inhibition and DHODH inhibition both at the level of regulating glutamine levels and (at least for some GLS1 inhibitors) at the level of growth and survival. One hypothesis that accounts for the current observations is that DHODH activity helps to mediate the balance between two distinct glutaminolysis-dependent redox metabolic pathways that have been implicated in growth/survival in *KRAS* mutant cells: generation of mitochondrial reactive oxygen species (ROS) (Weinberg et al., 2010) and flux through GOT1 enabling generation of NADPH and maintenance of reduced glutathione (Son et al., 2013; Yun et al., 2015).

Electron transport via DHODH activity will allow the generation of mitochondrial ROS without the consumption of α-ketoglutarate or NADH. Glutamine-dependent flux through the TCA cycle and oxidative phosphorylation can also enable generation of mitochondrial ROS (Weinberg et al., 2010). The latter process requires partitioning of αKG derived from glutamine into the TCA cycle to generate reducing equivalents in the form of NADH, leading ultimately to reduction of molecular oxygen by Complex III to generate ROS (Weinberg et al., 2010). However, since production of NADPH via GOT1/MDH1/ME1 (Son et al., 2013; Yun et al., 2015) also requires consumption of αKG and NADH, these metabolites must partition between the two pro-survival pathways. DHODH activity may thus be required to enable high flux through both of these pathways simultaneously.

KRAS mutant cells, unlike WT cells, also exhibit a large brequinar-mediated increase in fructose-1,6-bisphosphate levels (Figure S7). However, there does not appear to be a clear mechanism for DHODH inhibition to mediate this effect directly. One possibility is that developing arrest of the cells in S phase leads to upregulation of glycolytic flux (Kaplon et al., 2015) and an increase in fructose-1,6-bisphosphate (which is downstream of the rate-limiting enzymes in this pathway). In that case, the upregulation of glycolytic flux would appear to be mostly through the anaerobic (lactic acid) branch of the pathway; brequinar treatment is associated with a decrease in the steady-state level of citrate without a concomitant decrease of isotopic exchange into this metabolite (Figure S7), suggesting a decreased flux of metabolites into the citric acid cycle.

The relative functional importance of DHODH's pyrimidine biosynthetic, energy-producing, and redox-modulating functions is likely to depend on cellular context. DHODH has previously been characterized as a synthetic lethal target in several different oncogenic cell contexts, including the *BRAF* V600E mutation (White et al., 2011), PTEN deficiency (Mathur et al., 2017), and triple-negative breast cancer cell lines (Brown et al., 2017). In the case of the *BRAF* V600E mutation, oncogenic mutations of both *BRAF* and *KRAS* are gain-of-function with respect to the Ras-Raf-MEK-ERK pathway, which may account for the shared phenotype with respect to DHODH inhibition. However, KRAS signaling affects multiple signaling pathways in addition to Raf-MEK-ERK, so, in general, interventions that affect *KRAS* mutant cells may or may not affect *BRAF* mutant cells. Recently, *de novo* pyrimidine metabolism through carbamoyl phosphate generated in the urea cycle has been shown to be important for growth/survival in the *KRAS/LKB1* double-mutant context (Kim et al., 2017), suggesting that DHODH inhibition might be useful specifically in this cellular context as well.

The *in vitro* and *in vivo* results presented here suggest that DHODH inhibition may be clinically useful in the treatment of *KRAS* mutant tumors. However, in previous clinical trials, brequinar failed to demonstrate efficacy in multiple tumor types, including pancreatic and colorectal, a substantial fraction of which almost certainly harbored *KRAS* mutations (Moore et al., 1993; Peters et al., 1992). Understanding the basis for the discrepancy between *in vitro/in vivo* models and clinical results might enable the design of new and more effective clinical treatment strategies.

One possible explanation for the lack of observed clinical effectiveness for brequinar is that target engagement in the clinical studies was insufficient to induce tumor cell death. *In vivo* studies suggest that prolonged exposure to brequinar is required to achieve the metabolite depletion effects required for maximum efficacy (Dexter et al., 1985; Schwartsmann et al., 1988). However, the clinical trials of brequinar were designed following a traditional chemotherapeutic regimen, in which the maximum tolerated dose was delivered, followed by an intervening recovery period. Pharmacokinetic data from these clinical trials (Arteaga et al., 1989) reveals that between doses, the plasma drug concentrations dropped below the efficacy threshold seen in our preclinical studies, and investigators in

the clinical studies speculated that maintaining effective drug concentrations over a longer period of time might be required to achieve clinical efficacy (Braakhuis et al., 1990).

Another potential approach to achieving clinical benefit from DHODH inhibition would be to employ combination therapies. The results reported here suggest that promising combination candidates include floxuridine (an inhibitor of pyrimidine biosynthesis via thymidylate synthase) and gemcitabine (an inhibitor of ribonucleotide reductase), both of which also target nucleotide metabolism. Gemcitabine is a particularly intriguing potential combination partner because it is already in use as a first-line therapy for pancreatic cancer. Results on GLS1 inhibitors suggest that such agents might also be useful combination agents for DHODH inhibitors, although highly potent GLS1 inhibitors may be required for a synergistic effect to be observable at the level of growth inhibition.

The current study provides evidence for a previously unknown role for DHODH as a growth/survival factor in *KRAS* mutant tumors. While many aspects of the link between DHODH inhibition and survival of *KRAS* mutant cells remain to be established, *de novo* pyrimidine biosynthesis appears to be a crucial pathway for *KRAS* mutant cells. The connection between *KRAS* mutant status and a requirement for DHODH enzymatic activity may enable new therapeutic approaches for *KRAS* mutant cancers.

SIGNIFICANCE

A synthetic lethal screen for small molecules that selectively inhibit the growth of *KRAS* mutant cell lines identifies inhibitors of dihydroorotate dehydrogenase (DHODH) as potential therapies for *KRAS* mutant cancers. An investigation of the metabolic effects of these inhibitors on *KRAS* mutant cell lines points to perturbation of primary energy metabolism and glutamine metabolism as possible contributors to the observed *KRAS* mutant selectivity. The results suggest that alternative clinical trial designs for potent clinical-stage DHODH inhibitors such as brequinar in *KRAS* mutant cancers may be worth evaluating.

STAR★METHODS

Detailed methods are provided in the online version of this paper and include the following:

- KEY RESOURCES TABLE
- CONTACT FOR REAGENT AND RESOURCE SHARING
- EXPERIMENTAL MODEL AND SUBJECT DETAILS
  - *In Vivo* Animal Studies
  - Cell Lines
- METHOD DETAILS
  - Reagents
  - Compound Screening in 3D Cultures
  - KRAS Knockdown: shRNA Expression and Gene Down-Regulation
  - Cell Line Sensitivity Profiling
  - Biochemical Pull-Down Experiment with Thiazolimine-Conjugated Beads
  - SDS/PAGE and In-Gel Digestion
  - iTRAQ Labeling of the Digested Pull-Down Samples
  - Mass Spectrometry Analysis and Data Interpretation
  - DHODH Biochemical Assay
  - Cell Cycle Analysis
  - Mitochondrial Membrane Potential Assay
  - LC-MS/MS Mass Spectrometric Metabolite Analysis of Cells and Tumor Tissues
  - CE-TOFMS Mass Spectrometric Metabolite Analysis of Cells and Tumor Tissues
  - Synergistic Combinations in KRAS Mutant Cell Context
  - General Synthetic Methods
  - Synthetic Protocols
- QUANTIFICATION AND STATISTICAL ANALYSIS

SUPPLEMENTAL INFORMATION

Supplemental Information includes seven figures and one table can be found with this article online at https://doi.org/10.1016/j.chembiol.2018.03.005.

ACKNOWLEDGMENTS

We thank Dr. Laura Shelton (Human Metabolome Technologies) for helpful discussions. We thank Dr. Dietmar Hoffmann and the Sanofi Molecular Cloning group for generation of inducible shRNA vectors for *KRAS* knockdown. We thank Dr. Joern Hopke for microscopic image acquisition and analysis.

AUTHOR CONTRIBUTIONS

M.K., J.S., A.C., B.L., G.T., L.B., I.M., I.S, C.P., S.V., B.B., B.Z., T.H., Q.G., P.G, D.S., M.P.C., R.T., M. Barrague, R.N., Y.W., F.S., J.M., E.Y., and D.H. designed and carried out experiments. S.R., H.C., M.M., E.Y., and J.P. analyzed data. M. Barrague, M. Bouaboula, J.P., C.G., C. G-E., H.C., F.A., C.W., S.L., I. C-T. R.A., and A.M. designed and interpreted experiments. M.K., J.S., B.Z., Q.G., D.S., R.N., S.L., and A.M. wrote the manuscript, with contributions from all other authors.

DECLARATION OF INTERESTS

The authors are current or former employees and/or shareholders of Sanofi.

Received: November 23, 2016
Revised: December 29, 2017
Accepted: March 8, 2018
Published: April 5, 2018

REFERENCES

Arteaga, C.L., Brown, T.D., Kuhn, J.G., Shen, H.S., O'Rourke, T.J., Beougher, K., Brentzel, H.J., Von Hoff, D.D., and Weiss, G.R. (1989). Phase I clinical and pharmacokinetic trial of brequinar sodium (DuP 785; NSC 368390). Cancer Res. *49*, 4648–4653.

Bantscheff, M., Eberhard, D., Abraham, Y., Bastuck, S., Boesche, M., Hobson, S., Mathieson, T., Perrin, J., Raida, M., Rau, C., et al. (2007). Quantitative chemical proteomics reveals mechanisms of action of clinical ABL kinase inhibitors. Nat. Biotechnol. *25*, 1035–1044.

Barbie, D.A., Tamayo, P., Boehm, J.S., Kim, S.Y., Moody, S.E., Dunn, I.F., Schinzel, A.C., Sandy, P., Meylan, E., Scholl, C., et al. (2009). Systematic RNA interference reveals that oncogenic KRAS-driven cancers require TBK1. Nature *462*, 108–112.

Bardeesy, N., and DePinho, R.A. (2002). Pancreatic cancer biology and genetics. Nat. Rev. Cancer *2*, 897–909.

Ben-Sahra, I., Howell, J.J., Asara, J.M., and Manning, B.D. (2013). Stimulation of *de novo* pyrimidine synthesis by growth signaling through mTOR and S6K1. Science *339*, 1323–1328.

Berenbaum, M.C. (1989). What is synergy? Pharmacol. Rev. *41*, 93–141.

Bliss, C.I. (1939). The toxicity of poisons applied jointly. Ann. Appl. Biol. *26*, 585–615.

Braakhuis, B.J., van Dongen, G.A., Peters, G.J., van Walsum, M., and Snow, G.B. (1990). Antitumor activity of brequinar sodium (Dup-785) against human head and neck squamous cell carcinoma xenografts. Cancer Lett. *49*, 133–137.

Brown, K.K., Spinelli, J.B., Asara, J.M., and Toker, A. (2017). Adaptive reprogramming of *de novo* pyrimidine biosynthesis is a metabolic vulnerability in triple-negative breast cancer. Cancer Discov. *7*, 391–399.

Campbell, P.M., Groehler, A.L., Lee, K.M., Ouellette, M.M., Khazak, V., and Der, C.J. (2007). K-Ras promotes growth transformation and invasion of immortalized human pancreatic cells by Raf and phosphatidylinositol 3-kinase signaling. Cancer Res. *67*, 2098–2106.

Chen, S.F., Perrella, F.W., Behrens, D.L., and Papp, L.M. (1992). Inhibition of dihydroorotate dehydrogenase activity by brequinar sodium. Cancer Res. *52*, 3521–3527.

Chou, T.C., and Talalay, P. (1984). Quantitative analysis of dose-effect relationships: the combined effects of multiple drugs or enzyme inhibitors. Adv. Enzyme Regul. *22*, 27–55.

Connolly, G.P., and Duley, J.A. (1999). Uridine and its nucleotides: biological actions, therapeutic potentials. Trends Pharmacol. Sci. *20*, 218–225.

Cox, A.D., Fesik, S.W., Kimmelman, A.C., Luo, J., and Der, C.J. (2014). Drugging the undruggable RAS: mission possible? Nat. Rev. Drug Discov. *13*, 828–851.

Davis, J.P., Cain, G.A., Pitts, W.J., Magolda, R.L., and Copeland, R.A. (1996). The immunosuppressive metabolite of leflunomide is a potent inhibitor of human dihydroorotate dehydrogenase. Biochemistry *35*, 1270–1273.

Dexter, D.L., Hesson, D.P., Ardecky, R.J., Rao, G.V., Tippett, D.L., Dusak, B.A., Paull, K.D., Plowman, J., DeLarco, B.M., Narayanan, V.L., et al. (1985). Activity of a novel 4-quinolinecarboxylic acid, NSC 368390 [6-fluoro-2-(2'-fluoro-1,1'-biphenyl-4-yl)-3-methyl-4-quinolinecarb oxylic acid sodium salt], against experimental tumors. Cancer Res. *45*, 5563–5568.

Erra, M., Moreno, I., Sanahuja, J., Andres, M., Reinoso, R.F., Lozoya, E., Pizcueta, P., Godessart, N., and Castro-Palomino, J.C. (2011). Biaryl analogues of teriflunomide as potent DHODH inhibitors. Bioorg. Med. Chem. Lett. *21*, 7268–7272.

Graves, L.M., Guy, H.I., Kozlowski, P., Huang, M., Lazarowski, E., Pope, R.M., Collins, M.A., Dahlstrand, E.N., Earp, H.S., 3rd, and Evans, D.R. (2000). Regulation of carbamoyl phosphate synthetase by MAP kinase. Nature *403*, 328–332.

Gross, M.I., Demo, S.D., Dennison, J.B., Chen, L., Chernov-Rogan, T., Goyal, B., Janes, J.R., Laidig, G.J., Lewis, E.R., Li, J., et al. (2014). Antitumor activity of the glutaminase inhibtor CB-839 in triple-negative breast cancer. Mol. Cancer Ther. *13*, 890–901.

Guerrero, S., Casanova, I., Farre, L., Mazo, A., Capella, G., and Mangues, R. (2000). K-ras codon 12 mutation induces higher level of resistance to apoptosis and predisposition to anchorage-independent growth than codon 13 mutation or proto-oncogene overexpression. Cancer Res. *60*, 6750–6756.

Hesson, D.P. (1987). 2-Phenyl-4-quinolinecarboxylic acids and pharmaceutical compositions thereof. US patent US4680299A, filed July 14, 1987.

Hunter, J.C., Gurbani, D., Ficarro, S.B., Carrasco, M.A., Lim, S.M., Choi, H.G., Xie, T., Marto, J.A., Chen, Z., Gray, N.S., et al. (2014). *In situ* selectivity profiling and crystal structure of SML-8-73-1, an active site inhibitor of oncogenic K-Ras G12C. Proc. Natl. Acad. Sci. USA *111*, 8895–8900.

Kaplon, J., van Dam, L., and Peeper, D. (2015). Two-way communication between the metabolic and cell cycle machineries: the molecular basis. Cell Cycle *14*, 2022–2032.

Kim, J., McMillan, E., Kim, H.S., Venkateswaran, N., Makkar, G., Rodriguez-Canales, J., Villalobos, P., Neggers, J.E., Mendiratta, S., Wei, S., et al. (2016). XPO1-dependent nuclear export is a druggable vulnerability in KRAS-mutant lung cancer. Nature *538*, 114–117.

Kim, J., Hu, Z., Cai, L., Li, K., Choi, E., Faubert, B., Bezwada, D., Rodriguez-Canales, J., Villalobos, P., Lin, Y.F., et al. (2017). CPS1 maintains pyrimidine pools and DNA synthesis in KRAS/LKB1 mutant lung cancer cells. Nature *546*, 168–172.

Lemasters, J.J., Nieminen, A.L., Qian, T., Trost, L.C., Elmore, S.P., Nishimura, Y., Crowe, R.A., Cascio, W.E., Bradham, C.A., Brenner, D.A., et al. (1998). The mitochondrial permeability transition in cell death: a common mechanism in necrosis, apoptosis and autophagy. Biochim. Biophys. Acta *1366*, 177–196.

Linardou, H., Dahabreh, I.J., Kanaloupiti, D., Siannis, F., Bafaloukos, D., Kosmidis, P., Papadimitriou, C.A., and Murray, S. (2008). Assessment of somatic k-RAS mutations as a mechanism associated with resistance to EGFR-targeted agents: a systematic review and meta-analysis of studies in advanced non-small-cell lung cancer and metastatic colorectal cancer. Lancet Oncol. *9*, 962–972.

Luo, J., Emanuele, M.J., Li, D., Creighton, C.J., Schlabach, M.R., Westbrook, T.F., Wong, K.K., and Elledge, S.J. (2009). A genome-wide RNAi screen identifies multiple synthetic lethal interactions with the Ras oncogene. Cell *137*, 835–848.

Mann, M. (2006). Functional and quantitative proteomics using SILAC. Nat. Rev. Mol. Cell Biol. *7*, 952–958.

Mathur, D., Stratikopoulos, E., Ozturk, S., Steinbach, N., Pegno, S., Schoenfeld, S., Yong, R., Murty, V.V., Asara, J.M., Cantley, L.C., and Parsons, R. (2017). PTEN regulates glutamine flux to pyrimidine synthesis and sensitivity to dihydroorotate dehydrogenase inhibition. Cancer Discov. *7*, 380–390.

McLean, J.E., Neidhardt, E.A., Grossman, T.H., and Hedstrom, L. (2001). Multiple inhibitor analysis of the brequinar and leflunomide binding sites on human dihydroorotate dehydrogenase. Biochemistry *40*, 2194–2200.

Moore, M., Maroun, J., Robert, F., Natale, R., Neidhart, J., Dallaire, B., Sisk, R., and Gyves, J. (1993). Multicenter phase II study of brequinar sodium in patients with advanced gastrointestinal cancer. Invest. New Drugs *11*, 61–65.

Ostrem, J.M., Peters, U., Sos, M.L., Wells, J.A., and Shokat, K.M. (2013). K-Ras(G12C) inhibitors allosterically control GTP affinity and effector interactions. Nature *503*, 548–551.

Patel, D., Menon, D., Bernfeld, E., Mroz, V., Kalan, S., Loayza, D., and Foster, D.A. (2016). Aspartate rescues S-phase arrest caused by suppression of glutamine utilization in KRas-driven cancer cells. J. Biol. Chem. *291*, 9322–9329.

Peters, G.J., Kraal, I., and Pinedo, H.M. (1992). *In vitro* and *in vivo* studies on the combination of brequinar sodium (DUP-785; NSC 368390) with 5-fluorouracil; effects of uridine. Br. J. Cancer *65*, 229–233.

Peters, G.J., Schwartsmann, G., Nadal, J.C., Laurensse, E.J., van Groeningen, C.J., van der Vijgh, W.J., and Pinedo, H.M. (1990). *In vivo* inhibition of the pyrimidine *de novo* enzyme dihydroorotic acid dehydrogenase by brequinar sodium (DUP-785; NSC 368390) in mice and patients. Cancer Res. *50*, 4644–4649.

Robitaille, A.M., Christen, S., Shimobayashi, M., Cornu, M., Fava, L.L., Moes, S., Prescianotto-Baschong, C., Sauer, U., Jenoe, P., and Hall, M.N. (2013). Quantitative phosphoproteomics reveal mTORC1 activates de novo pyrimidine synthesis. Science *339*, 1320–1323.

Scholl, C., Frohling, S., Dunn, I.F., Schinzel, A.C., Barbie, D.A., Kim, S.Y., Silver, S.J., Tamayo, P., Wadlow, R.C., Ramaswamy, S., et al. (2009). Synthetic lethal interaction between oncogenic KRAS dependency and STK33 suppression in human cancer cells. Cell *137*, 821–834.

Schwartsmann, G., Peters, G.J., Laurensse, E., de Waal, F.C., Loonen, A.H., Leyva, A., and Pinedo, H.M. (1988). DUP 785 (NSC 368390): schedule-dependency of growth-inhibitory and antipyrimidine effects. Biochem. Pharmacol. *37*, 3257–3266.

Shaw, A.T., Winslow, M.M., Magendantz, M., Ouyang, C., Dowdle, J., Subramanian, A., Lewis, T.A., Maglathin, R.L., Tolliday, N., and Jacks, T. (2011). Selective killing of K-ras mutant cancer cells by small molecule inducers of oxidative stress. Proc. Natl. Acad. Sci. USA *108*, 8773–8778.

Son, J., Lyssiotis, C.A., Ying, H., Wang, X., Hua, S., Ligorio, M., Perera, R.M., Ferrone, C.R., Mullarky, E., Shyh-Chang, N., et al. (2013). Glutamine supports pancreatic cancer growth through a KRAS-regulated metabolic pathway. Nature *496*, 101–105.

Steckel, M., Molina-Arcas, M., Weigelt, B., Marani, M., Warne, P.H., Kuznetsov, H., Kelly, G., Saunders, B., Howell, M., Downward, J., et al. (2012). Determination of synthetic lethal interactions in KRAS oncogene-dependent cancer cells reveals novel therapeutic targeting strategies. Cell Res. *22*, 1227–1245.

Sun, Q., Burke, J.P., Phan, J., Burns, M.C., Olejniczak, E.T., Waterson, A.G., Lee, T., Rossanese, O.W., and Fesik, S.W. (2012). Discovery of small molecules that bind to K-Ras and inhibit Sos-mediated activation. Angew. Chem. Int. Ed. *51*, 6140–6143.

van der Windt, G.J.W., Everts, B., Chang, C.-H., Curtis, J.D., Freitas, T.C., Amiel, E., Pearce, E.J., and Pearce, E.L. (2012). Mitochondrial respiratory capacity is a critical regulator of $CD8^+$ T cell memory development. Immunity *36*, 68–78.

Viale, A., Pettazzoni, P., Lyssiotis, C.A., Ying, H., Sanchez, N., Marchesini, M., Carugo, A., Green, T., Seth, S., Giuliani, V., et al. (2014). Oncogene ablation-resistant pancreatic cancer cells depend on mitochondrial function. Nature *514*, 628–632.

Weinberg, F., Hamanaka, R., Wheaton, W.W., Weinberg, S., Joseph, J., Lopez, M., Kalyanaraman, B., Mutlu, G.M., Budinger, G.R., and Chandel, N.S. (2010). Mitochondrial metabolism and ROS generation are essential for Kras-mediated tumorigenicity. Proc. Natl. Acad. Sci. USA *107*, 8788–8793.

White, R.M., Cech, J., Ratanasirintrawoot, S., Lin, C.Y., Rahl, P.B., Burke, C.J., Langdon, E., Tomlinson, M.L., Mosher, J., Kaufman, C., et al. (2011). DHODH modulates transcriptional elongation in the neural crest and melanoma. Nature *471*, 518–522.

Ying, H., Kimmelman, A.C., Lyssiotis, C.A., Hua, S., Chu, G.C., Fletcher-Sananikone, E., Locasale, J.W., Son, J., Zhang, H., Coloff, J.L., et al. (2012). Oncogenic Kras maintains pancreatic tumors through regulation of anabolic glucose metabolism. Cell *149*, 656–670.

Yun, J., Mullarky, E., Lu, C., Bosch, K.N., Kavalier, A., Rivera, K., Roper, J., Chio, , II, Giannopoulou, E.G., Rago, C., et al. (2015). Vitamin C selectively kills KRAS and BRAF mutant colorectal cancer cells by targeting GAPDH. Science *350*, 1391–1396.

STAR★METHODS

KEY RESOURCES TABLE

REAGENT or RESOURCE	SOURCE	IDENTIFIER
Antibodies		
Anti-Ras Antibody, clone RAS10	Millipore Sigma	Cat#05-516; RRID: AB_11211664
Monoclonal Anti-β-Actin	Millipore Sigma	Cat#A5316; RRID: AB_476743
Chemicals, Peptides, and Recombinant Proteins		
Recombinant DHODH	Creative Biomart	Cat#DHODH-2486
PD0325901 MEK Inhibitor	Selleck Chemicals	Cat#S1036
Pimasertib (AS-703026) MEK Inhibitor	Selleck Chemicals	Cat#S1475
Brequinar	Sanofi internal collection	N/A
Teriflunomide	Sanofi internal collection	N/A
Floxuridine	Selleck Chemicals	Cat#S1299
Gemcitabine	Selleck Chemicals	Cat#S1149
Everolimus (RAD001)	Selleck Chemicals	Cat#S1120
Staurosporine	Sigma	Cat#62996-74-1
SeaPrep Agarose	Lonza	Cat#50302
Hoeschst 35480	Invitrogen	Cat#H21486
MitoTracker Red	Thermofisher	Cat#M7512
Critical Commercial Assays		
Trans-Lentiviral shRNA Packaging Kit	Open Biosystems	Cat#TLP5912
KRAS Taqman Gene Expression assay	Thermofisher	Cat#Hs00270666_m1
β Actin Taqman Gene Expression assay	Thermofisher	Cat#Hs01102345_m1
TaqMan Gene Expression Cells-to-CT Kit	Thermofisher	Cat#AM1729
iTRAQ® Reagents	SCIEX	iTRAQ® Reagents
Cell Titer Glo	Promega	Cat#G7570
Experimental Models: Cell Lines		
KP-4	JCRB	JCRB0182
DLD-1	ATCC	ATCC CCL-221
PANC-1	ATCC	ATCC CRL-1469
CFPAC-1	ATCC	ATCC CRL-1918
HCT116	ATCC	ATCC CCL-247
MIA PaCa-2	ATCC	ATCC CRL-1420
H1299	ATCC	ATCC CRL-5803
UISO-BCA-1	Southern Research Institute	CVCL_D249
ACHN	ATCC	ATCC CRL-1611
SK-OV-3	ATCC	ATCC HTB-77
DLD1 KRAS (+/-)	Horizon Discovery	HD 105-002
DLD1 KRAS (G13D/-)	Horizon Discovery	HD 105-011
Experimental Models: Organisms/Strains		
Female SCID mice	Charles River Laboratories	N/A
Oligonucleotides		
shRNA KRAS B sequence : CACCGTT GGAGCTGGTGGtGTgGGCTTCAA GAGAGCCTACGCCACCAGCTCCAAC	This paper, Sanofi	N/A
shRNA KRAS H sequence : CACCGGT CCTGCTGACAAATCAgGATTCAAGAG ATCTTGATTTGTCAGCAGGACC	This paper, Sanofi	N/A

(*Continued on next page*)

Continued		
REAGENT or RESOURCE	SOURCE	IDENTIFIER
Recombinant DNA		
pLKO_IRES-Puro_DEST	Sanofi internal collection	N/A
Other		
Ultra low-attachment 384 well plates	Corning	Cat#3827

CONTACT FOR REAGENT AND RESOURCE SHARING

Further information and requests for resources and reagents should be directed to and will be fulfilled by the Lead Contact, Stuart Licht (sslicht@gmail.com).

EXPERIMENTAL MODEL AND SUBJECT DETAILS

In Vivo Animal Studies

All *in vivo* experiments were performed according to institutional guidelines as approved by the Sanofi Institutional Animal Care and Use Committee. $5x10^6$ KP-4 cells were suspended in 50% matrigel and 50%DPBS and implanted subcutaneously into the right flank of 7∼8 week old female Severe Combined Immuno Deficiency (SCID) mice (Charles River Laboratories). The tumors were allowed to establish until average tumor volume reached about 200-250 mm^3. Subsequently mice were randomized into control and treated groups (n=10/group), Tumor growth was monitored over time using caliper measurements. Subcutaneous tumor volume was calculated using the formula: length × $width^2/2$. Brequinar was formulated in 20% HPbCD in 10mM phosphate buffer. Animals were orally administered brequinar at 1, 3, 10, 30 mg/kg once daily for 14 days. For the pharmacodynamic studies (Figures 6A–6C), three mice were used for each time point. In the efficacy study (Figure 6D), ten mice were used in each group.

Cell Lines

The following cell lines were used as a panel for initial testing in soft agar : PANC-1 (pancreatic), KP-4 (pancreatic), CFPAC-1 (pancreatic), MiaPaCa-2 (pancreatic), HCT-116 (colon), DLD-1 (colon), SK-OV-3 (ovarian), ACHN (kidney), H1299 (lung), UISO-BCA-1 (breast). Chemoproteomic experiments, cell cycle analysis, mitochondrial potential experiments, metabolite profiling, and drug synergy experiments were carried out using KP-4 cells. For capillary electrophoresis-based metabolomics experiments, DLD-1 cells bearing either a single mutant or single wild-type allele were used (DLD1 KRAS (+/-) HD-105-002 and DLD1 KRAS (G13D/-) HD-105-011, Horizon Discovery). All cells were cultured at 37°C in humidified incubators at 5% CO_2.

METHOD DETAILS

Reagents

Biochemical reagents were obtained from Sigma-Aldrich unless otherwise specified. Brequinar was synthesized as previously described (Hesson, 1987). MEK inhibitor PD0325901 was purchased from Selleck Chemicals.

Compound Screening in 3D Cultures

SeaPrep agarose (Lonza #50302) was used for cell culture. A 6% (w/v) agarose solution in PBS (Gibco#10010) was prepared by mixing the components in an autoclavable bottle via magnetic stirring. The suspension was autoclaved, then stirred again until homogeneous. The final concentration diluted in media for cell culture was 1%; volumes of the 6% stock solution (1.05 g/mL) were measured gravimetrically.

For assay purposes, a mixture of cells and agarose (final concentration of agarose 1% in complete media, 40,000 cells/ml) was prepared from cell and agarose stocks pre-warmed to 37°C, and kept at 37°C until it was dispensed via an automated liquid handling system (Thermo Scientific Multidrop Combi) into 384-well ultra low-attachment plates (Corning, #3827); low-attachment plates were used to ensure that any cells that settle will remain rounded rather than attaching to the plate, such plates eliminate the need for the traditional bottom agar layer. The plates were incubated at 4°C for 15-30 minutes to allow gelling to occur. After gelling of the agarose, the cultures were incubated at 5% CO_2 and 37°C in a humidified incubator. Clonogenicity of cell lines was determined using this culture system for cell lines of interest.

Compound plates for screening were prepared in advance using acoustic dispensing (Labcyte Echo). On day 4 after plating of cells, compounds to be screened (in DMSO stock) were diluted in media and added to the culture plates using an automated liquid dispenser (BioMek FX). On day 7 after plating of cells,Alamar Blue dye (10 μl) was added to culture plates using an automated liquid dispenser (BioMek FX), and the plates were incubated at 37°C (incubation periods were optimized for each cell line to maximize the

fluorescence signal and avoid reagent depletion). Fluorescence (Ex/Em 530 nm/590 nm) was measured (Envision 2104 multi-label reader) to determine cell viability.

KRAS Knockdown: shRNA Expression and Gene Down-Regulation

shRNAs against *KRAS* were cloned in a Tet-inducible pLKO vector (pLKO_IRES_Puro_Dest). The shRNA sequences used were the following: shRNA KRAS B, CACCGTTGGAGCTGGTGGtGTgGGCTTCAAGAGAGCCTACGCCACCAGCTCCAAC ; shRNA KRAS H, CACCGGTCCTGCTGACAAATCAgGATTCAAGAGATCTTGATTTGTCAGCAGGACC.

The shRNA-expressing lentiviral vectors were packaged in 293T cells using the Trans-Lentiviral packaging kit (OpenBiosystems). Culture medium containing virus was collected and filtered. Cells were transduced with virus and subjected to puromycin selection. After selection, the surviving cells were grown in 3D culture as previously described, and doxycycline was added to the culture to induce shRNA expression. Cells were re-fed with doxycycline every 2 or 3 days.

Downregulation of *KRAS* at the mRNA level was determined using a KRAS Taqman Gene Expression assay - Hs00270666_m1 (Thermofisher) and Cells-To-Ct kit (Ambion/ABI, #4399002). RPL37A - Hs01102345_m1 (ThermoFisher) was used as a housekeeping gene for normalization. Cells were plated in a 96-well format. Seventy-two hours after shRNA induction, cells were washed with 1X PBS. cDNA preparation from cell lysates and qPCR were carried out according to the manufacturer's instructions.

To determine down-regulation of KRAS protein, cells were plated in 6-well plates. Seventy-two hours after shRNA induction, the cells were washed with 1X PBS and lysed in 1X RIPA lysis buffer (Thermo 89901) containing 1X Halt Protease and phosphatase inhibitor (Thermo 78440). Samples were run on NuPage Novex 4-12% Bis-Tris polyacrylamide protein gels, and transferred to membranes using the iBlot system (Invitrogen). Membranes were incubated with an anti-Ras antibody (Millipore Sigma #: 05-516) and probed using secondary antibodies (LiCOR). β-actin (Millipore sigma #A5316) was used a loading control.

Cell Line Sensitivity Profiling

A set of 640 mechanistically diverse compounds were obtained from commercial sources or an internal library. A total of 374 cancer cell lines of diverse origin were obtained from commercial vendors. Cell lines were chosen to sample diverse gene expression profiles. The cell lines represented 27 tissue types, with some lineages, such as liver, lung, pancreas, and stomach, being more highly represented. The cell lines were cultured in vendor-recommended media using standard culturing techniques, either in a biological safety cabinet or using an automated cell culture system (CompacT, Sartorius, Wilmington DE.). For dose-response studies, all compounds were dissolved in DMSO and diluted in an 8-point dilution series, and an aliquot (10 μL) of each dilution was placed in a Labcyte-certified LDV 384-well polystyrene plate. The starting stock concentrations used were between 0.1 mM to 10 mM, depending on compound activity, solubility, and availability.

To screen the compounds for bioactivity against the cell line panel, a Labcyte Echo (Sunnyvale CA) liquid dispensing system was used to transfer compound solution (25 nL) to 384-well assay plates (Greiner Bio-One, Monroe, NC). In addition to library compounds, each assay plate also contained DMSO vehicle controls and a staurosporine (Sigma, St Louis MO) positive control. All liquid dispensing and assay steps subsequent to the initial compound transfer were performed using a custom robotics platform (GNF, San Diego CA). Cell suspension (25 μL) was added to each well, using a seeding density between 250 and 1500 cells per well, depending on the cell line. Assay plates were incubated at 37°C for 72-168 hours. Cell numbers were determined by adding Hoechst34580 DNA staining dye (5 μL; Invitrogen) to a final concentration of 2 μg/mL. Assay plates were incubated for 3 hours at 37°C, 9% paraformaldehyde (10 μL; EMS Hatfield, PA) was added, and the plates were incubated at room temperature for 4 h. Following fixation, cell counts were determined using an Acumen microplate cytometer (TTP Labtech Cambridge MA). Cell number values were corrected for pattern artifacts, and normalized to the vehicle control and the number of untreated cells initially plated in order to quantify effects on growth inhibition; growth inhibition was calculated as (median cell number-treated/median cell number untreated)*100. All dose-response fitting was performed on normalized data using either a four-parameter logistic nonlinear regression model or a constant model (Genedata AG).

For DLD-1 cell lines, cells were plated at a density of 3000 cells/well and cultured for 2 days before drug and/or uridine treatment; after 72 hours of treatment, viable cell density was quantified using the CellTiter Glo assay (Promega).

A subset of data containing a matrix of growth inhibition potencies from 372 cell lines (53 of which contain mutant *KRAS*) and 489 compounds was used for the analysis of the effect of *KRAS* mutation status on compound bioactivity. A t-test was performed for each compound, comparing the mean of potencies in *KRAS*-mutant and wild-type cell lines. The Bonferroni correction for multiple comparisons was applied to the final p-values. The result is shown in a volcano plot. In a similar analysis, the effects of mutation status of multiple oncogenes on the potencies of the lead thiazolimine was also compared.

Biochemical Pull-Down Experiment with Thiazolimine-Conjugated Beads

Protein pull-down using chemically modified beads was performed as described previously (Bantscheff et al., 2007). KP-4 cells separately SILAC-labeled with either L-arginine and L-lysine (light) or L-arginine-$^{13}C_6$ and L-lysine-$^{13}C_6$-$^{15}N_2$ (heavy) were prepared in lysis buffer containing 1% Nonidet P-40, 50 mM Tris/HCl, pH 7.5, 5% glycerol, 1.5 mM $MgCl_2$, 150 mM NaCl, 1 mM EDTA, and protease inhibitors (Complete tablets, Roche Applied Science, IN). Lysates were vortexed intermittently and chilled on ice for 10 min, followed by centrifugation at 14,000×g. Protein concentrations of lysates were measured using the Protein BCA Assay (Thermo Pierce, CA),

and lysates were diluted to a final protein concentration of 5 mg/ml in the lysis buffer. The heavy amino acid-labeled cell lysate was pre-incubated with the active competitor compound Compound **2** (50 nM or 1 μM, in separate aliquots) for 1 h. The light amino acid-labeled cell lysate was treated with DMSO as a control. Beads conjugated with the thiazolimine (200 μl) were added to each lysate and incubated on an end-over-end rotator for 4 h at 4°C. After incubation, the bead/lysate mixture was centrifuged at 1000×g and the supernatant was aspirated. The beads from each lysate were washed with lysis buffer to remove excess soluble small molecule competitor. Beads from the heavy and light amino acid-labeled lysates were combined and washed (3X) with lysis buffer supplemented with 0.1% SDS buffer. After the final wash, beads were collected by centrifugation at 1000×g, and the residual buffer was carefully aspirated to avoid disturbing the beads.

SDS/PAGE and In-Gel Digestion

Proteins bound to thiazolimine-conjugated beads were reduced and alkylated on-bead in 10 mM DTT and 25 mM iodoacetamide respectively. NuPAGE LDS sample buffer (Invitrogen) was added to bead mixtures, followed by heating to 60°C for 40 min. Eluted proteins were resolved on a 4n) was added to bead Bis-Tris gel with MES running buffer (Nupage, Invitrogen), and stained with Coomassie Blue (Simply Blue, Invitrogen). Gel lanes were excised into twelve pieces, each of which was cut into 1 x 1 mm cubes. The gel pieces were further destained three times in a solution containing 50% acetonitrile and 50% ammonium bicarbonate (50 mM), then dehydrated in 100% acetonitrile and completely dried in a vacuum concentrator (SpeedVac, Thermo Scientific) before addition of sufficient trypsin solution (12.5 ng/L) to swell the gel pieces. The gel pieces were incubated in the trypsin solution at 37°C overnight. The peptides were extracted three times from the gel in 2:1 (vol/vol) acetonitrile/5% formic acid and dried in a vacuum concentrator to remove organic solvents. The peptides were re-dissolved in an aqueous solution containing 0.1% formic acid and 5% acetonitrile for mass spectrometry analysis.

iTRAQ Labeling of the Digested Pull-Down Samples

iTRAQ labeling was performed using the iTRAQ Reagent kit (AB SCIEX, CA) according to the manufacturer's instructions. The peptides extracted from the SDS-PAGE gel were dried and reconstituted in the labeling buffer (0.5 M tetraethylammonium bromide) provided with the kit. The peptides from the control lysate (treated with DMSO) were labeled with iTRAQ reagent 114, and the peptides from lysate treated with 10 nM, 100 nM and 1 μM active competitor Compound **2** were labeled with iTRAQ reagents 115, 116, and 117, respectively. After labeling with iTRAQ reagents, the peptides were incubated at room temperature for 2 h and pooled.

Mass Spectrometry Analysis and Data Interpretation

LC-MS/MS analysis was carried out on a LTQ OrbitrapVelos mass spectrometer (Thermo Scientific, MA) equipped with a Thermo nanospray source (Thermo, San Jose, CA) and coupled to an Eksigent NanoLC Ultra 2D system (ABsciex). Separation of peptide mixtures was achieved on a 75 μm I.D. microcapillary trap column packed with 18 cm of Magic C18resin (3 μm, 200 Å, MichromBioresources) with a gradient of acetonitrile (3% -35%) in 0.1% FA for 145 minutes at a flow rate of 300 nL/min. A voltage of 3 kV was applied to generate electrospray. All the MS and MS/MS spectra were acquired in the data-dependent mode. The full-scan spectra (from m/z 300-1800) were acquired at resolution 60,000 at m/z 400, with an accumulation target value of 1 x 10^6. The top 20 most intense ions at a threshold above 500 counts were selected for fragmentation by CID at a normalized collision energy of 40%. Dynamic exclusion was applied to reject ions from repeated MS/MS selection for 90 ms using monoisotopic precursor selection. Singly-charged ions and those with unassigned charge state were also excluded from MS/MS.

The mass spectrometry data were processed using the Proteome Discoverer 1.3 software (Thermo Scientific). The MS/MS peak lists were extracted and searched by MASCOT against a concatenated forward and reversed version of the Swiss-prot human database. The precursor and fragment mass tolerances were set to 10 ppm and 0.5 Da, respectively. Cysteine carbamidomethylation was searched as a fixed modification, while N-acetyl protein, N-pyroglutamine, oxidized methionine, phosphorylation of serine, threonine, and tyrosine and SILAC labels on arginine and lysine were searched as variable modifications. The raw MS files were loaded to PD 1.3, and peptides were quantified with the MSQuant software embedded in the PD. MSQuant was used to calculate the ratio averaged over the peptide elution time, and the assignments used for quantification were visually displayed and validated. To minimize the false-discovery rate (FDR), all phosphopeptide identifications were filtered by MASCOT score. We accepted peptides based on the criterion that the number of forward hits in the database was at least 200-fold higher than the number of reversed database hits, which gives an estimated FDR of less than 1% ($p < 0.01$). The final filtering criteria were MASCOT score $\geq$ 20 ($p < 0.01$), identification of the peptide in the correct SILAC form (heavy or light), and presence of the correct number of lysine and arginine residues specified by the mass difference observed in the full scan between the SILAC partners.

DHODH Biochemical Assay

DHODH activity was measured using a coupled assay with 2,6-dichloroindophenol (DCIP) as the terminal electron acceptor. Reactions were carried out in UV-transparent plates (Corning #3675). The reaction mixture comprised HEPES buffer (100 mM, pH 7.5), sodium chloride (150 mM), Triton X-100 (0.01%), dihydroorotate (10 μM), decylubiquinone (10 μM), and DCIP (60 μM). The reaction was initiated by the addition of recombinant dihydroorotate dehydrogenase (5 nM, Creative Biomart part #DHODH-2486). Reaction progress was monitored by measuring the absorbance at 600 nm (extinction coefficient of the reduced DCIP product, 18.8 M^{-1} cm^{-1}; absorbance measured using an Envision 2104 plate reader equipped with a monochromator).

Cell Cycle Analysis

KP-4 cells were treated with Compound **2** or DMSO (vehicle control) for 24 or 48 h, then collected and fixed with ice-cold ethanol. Fixed cells were treated with RNAse, stained with propidium iodide, and subjected to flow cytometric analysis in duplicate to quantify DNA content.

Mitochondrial Membrane Potential Assay

KP-4 cells were treated with DHODH inhibitors at the defined concentrations for 72 h. After treatment, cells were stained with MitoTracker dye (ThermoFisher M7512; 300nM), washed with 1X PBS, fixed with paraformaldehyde (3.7%), and stained with Hoechst dye (Life Technologies H1399). Image acquisition was performed using a Perkin Elmer Opera QEHS automated microscope equipped with an Olympus 10X UPlanSApo objective. Hoechst33342 and Mitotracker Red CMXRos epifluorescence were detected using 450/50 nm and 600/40 nm bandpass filters, respectively, with excitation from 405 nm and 561 nm solid-state lasers. Mitochondrial depolarization was quantified by measuring the decrease in Mitotracker Red CMXRos relative fluorescence intensity (RFI). Fluorescene intensity data were analyzed using Perkin Elmer Columbus software: nuclei were segmented based on Hoechst staining, and through dilation of the nuclei segmentation mask, a ring region was created in which Mitotracker mean relative fluorescence intensity was calculated.

LC-MS/MS Mass Spectrometric Metabolite Analysis of Cells and Tumor Tissues

LC-MS/MS analysis was carried out using an ABSciex QTrap 5500 mass spectrometer coupled to a 1290 Infinity UHPLC system (Agilent). Samples were injected using a PAL HTC autosampler (LEAP Technologies). Separation of DHO and metabolites in the pyrimidine synthesis pathway was achieved on an ACQUITY UPLC CSH Fluoro-Phenyl column (50 mm × 2.1 mm, 1.7 μm Waters) at a flow rate of 0.50 ml/min. The elution protocol used was the following: holding mobile phase A (0.1% acetic acid in water) at 95% for 0.5 min; ramping mobile phase B (0.1% acetic acid in acetonitrile) from 5 to 95% over 4 min; holding mobile phase B at 90% for 0.5 min.

DHO and orotate were detected via their MRM transitions in the ESI negative mode; these were m/z 157 → 113 and m/z 155 → 111, for DHO and orotate, respectively. The transition for uridine was m/z 245 → 113 in the ESI positive mode. Instrument parameters were the following: spray voltage, 4000 V; source temperature, 450°C; ion source gas, 30 liter/h; and collision energy, 17 eV. Mass spectrometric data were acquired and processed using the Analyst software (ABSciex).

For analysis of cellular samples, cells were treated with compounds of interest for 24 h. Cell pellets (~1 million cells) were suspended in 80% methanol/water (500 μl) that had been chilled on dry ice. After brief sonication, the samples were centrifuged and the supernatants were collected. The pellets were resuspended in the methanol/water mixture used previously, and the extraction was repeated two additional times. The combined supernatants were dried in a centrifugal evaporator. The residues were reconstituted in water, and the resulting solutions were injected directly into the LC/MS-MS instrument for analysis of metabolites.

For samples from *in vivo* studies, tissue blocks were homogenized in 80% methanol/water (1 ml) using Precelly-24 with 2.8 mm ceramic beads (5500 rpm for 2 x 30 sec). The homogenate was centrifuged at 14000 rpm for 10 min and the supernatants were transferred. The methanol was removed by evaporation under vacuum, and the residue was reconstituted in water (2 ml) for the LC/MS/MS analysis.

CE-TOFMS Mass Spectrometric Metabolite Analysis of Cells and Tumor Tissues

DLD1 KRAS (+/-) HD-105-002 and DLD1 KRAS (G13D/-) HD-105-011 were obtained from Horizon Discovery. Cells were plated in RPMI 1640 with glutamine. Culture medium was aspirated the next day and cells treated with 2 μM Brequinar in absence or presence of 500 μM uridine in C^{13} glutamine labeled RPMI for 4 hours. For extraction of intracellular metabolites, culture medium was aspirated and cells were washed twice with a 5% mannitol solution. The cells were treated with 800 μL of methanol and 550 μL of Milli-Q water containing internal standards (H3304-1002, Human Metabolome Technologies, Inc., Tsuruoka, Japan). The extract was centrifuged at 2,300 ×*g* and 4°C for 5 min and then 800 μL of upper aqueous layer was centrifugally filtered through a Millipore 5-kDa cutoff filter at 9,100 ×*g* and 4°C for 120 min to remove proteins. The filtrate was centrifugally concentrated and re-suspended in 50 μL of Milli-Q water for CE-MS analysis.

Metabolome measurements were carried out through a facility service at Human Metabolome Technology Inc., Tsuruoka, Japan.

Hierarchical cluster analysis (HCA) and principal component analysis (PCA) were performed using proprietary software: PeakStat and SampleStat, respectively. Detected metabolites were plotted on metabolic pathway maps using VANTED (Visualization and Analysis of Networks containing Experimental Data) software.

Synergistic Combinations in KRAS Mutant Cell Context

A 12x12 dose matrix of co-plated enhancer and enhancee compounds was used to evaluate whether combination exhibited synergy. Cell culture was carried out in 2D format, as described in "Cell Line Sensitivity Profiling."

Compounds were diluted in a 12-point dilution series and dispensed in 40 μl aliquots into each well of a Labcyte-certified 384-well polypropylene plate. The enhancee compounds, brequinar and a DHODH inhibitor from the thiazolimine series (Compound **2**), were diluted and plated (in 25 nL aliquots) in the same format as the enhancer compounds using a Labcyte Echo (Sunnyvale CA) dispensing system. Cell culture and cell-based screening for growth inhibition effects (using KP-4 cells at a density of 500 cells/well, and a 72-hour treatment period) were carried out as described for "Cell Line Sensitivity Screening."

Three types of synergy scores, including Loewe, Bliss and HSA, were generated using software for analysis of *in vitro* pharmacology data (GeneData AG). For each type of synergy score (Loewe, Bliss, and HSA), a robust Z-test was performed to identify potential combination partners for Compound **2**. Specifically, a robust *Z* score was calculated for each compound combination as the difference between the synergy score from given combination and the median of synergy scores from self-cross experiments, divided by the median absolute deviation of synergy scores from self-cross experiments. The distributions of synergy scores from the self-cross experiments were found to be approximately normal for all three synergy score types, enabling the generation of two-tailed p values for each robust *Z* score. Since multiple robust Z tests were performed, multiple testing adjustment of p values was performed, using the Benjamini-Hochberg method. Any compound combination with a synergy score satisfying the criteria of Z > 0 and adjusted p value <= 0.05 was flagged as "synergistic."

General Synthetic Methods

Reagents and solvents were purchased from commercial sources and were used without further purification. All reactions were run under nitrogen atmosphere unless otherwise noted. Purification of reaction products was carried out by flash column chromatography using Teledyne Isco Combiflash Rf and Redisep normal-phase silica flash columns (230-400 mesh). Analytical thin layer chromatography was performed on EMD Millipore DC-Kieselgel 60 F_{254} plates. Visualization was accomplished with UV light, potassium permanganate, ninhydrin or Hanessian stain followed by heating. Proton nuclear magnetic resonance spectra (^{1}H NMR) were recorded on a Varian Inova 400MHz spectrometer and are reported in ppm using solvent as an internal standard (DMSO-d_6 at 2.50 ppm, methanol-d_4 at 3.31 ppm, acetone-d_6 at 2.09 ppm). Data are reported as br = broad peak, s = singlet, d = doublet, t = triplet, q = quadruplet, p = quintuplet, dd = doublet of doublets, ddd = doublet of doublet of doublets, m = multiplet; integration; coupling constant(s) in Hz. HPLC-MS analysis was carried out on a Waters Acquity UPLC® with autosampler, PDA detector and SQ mass spectrometer using Acquity UPLC® BEH C18 1.7um 2.1 x 50mm column. Preparative HPLC was performed on a Gilson Preparative HPLC system using a SunFire™ Prep C18 OBD™ 5uM 19x100mm column.

Synthetic Protocols

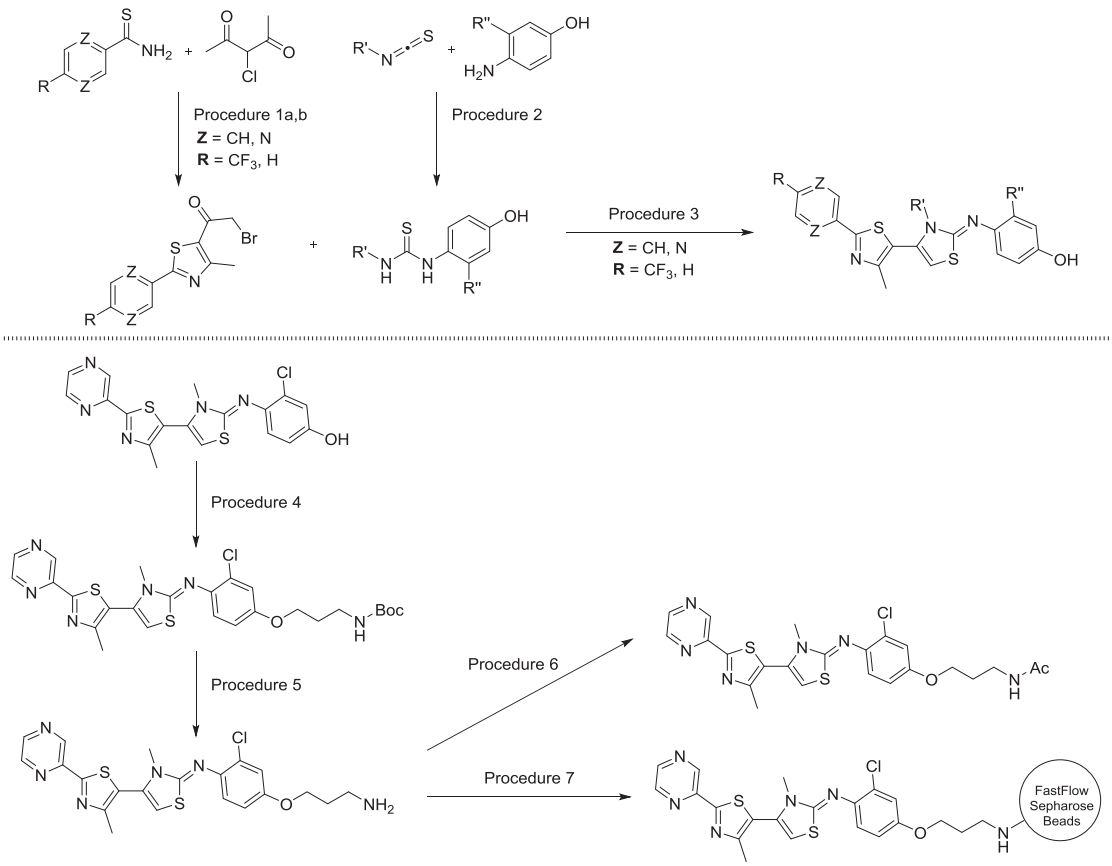

Scheme 1. Synthetic Routes

Procedure 1a

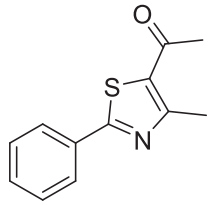

1-(4-Methyl-2-phenylthiazol-5-yl)ethanone (5)

To a solution of benzothioamide (5 g, 36.44 mmol) in ethanol (36.44 ml, 36.44 mmol) was added 3-chloro-2,4-pentanedione (4.24 ml, 36.44 mmol) at room temperature. The mixture was stirred at reflux for 4 h. An LC/MS indicated complete reaction. The mixture was allowed to cool down to room temperature. A precipitate formed. It was concentrated under reduced pressure. The residue was recrystallized from hexanes to provide 1-(4-methyl-2-phenylthiazol-5-yl)ethanone (3.6 g, 16.57 mmol, 45.5 % yield). **^{1}H NMR** (400 MHz, DMSO-d_6) δ 8.07 – 7.93 (m, 2H), 7.61 – 7.46 (m, 3H), 2.71 (s, 3H), 2.58 (s, 3H). **ESI-MS** *m/z* 218.2 [$(M + H)^+$; calcd. for $C_{12}H_{12}NOS$: 218.06].

Procedure 1b

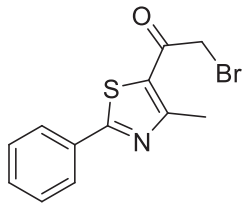

2-Bromo-1-(4-methyl-2-phenylthiazol-5-yl)ethan-1-one (6)

To a solution of 1-(4-methyl-2-phenylthiazol-5-yl)ethanone (3 g, 13.81 mmol) in dichloromethane (69.03 ml, 13.81 mmol) was added bromine (924.67 μl, 17.95 mmol). The solution was stirred at 40°C overnight. The mixture was concentrated under reduced pressure. The residue was triturated in methanol then dried under vacuum to give 2-bromo-1-(4-methyl-2-phenylthiazol-5-yl)ethan-1-one (3.26 g, 10.99 mmol, 79.6 %). **^{1}H NMR** (400 MHz, DMSO-d_6) δ 7.97 (m, 2H), 7.64 – 7.40 (m, 3H), 4.75 (s, 2H), 2.69 (s, 3H). **ESI-MS** *m/z* 296.1 [$(M + H)^+$; calcd. for $C_{12}H_{11}BrNOS$: 295.97].

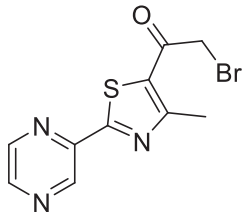

2-Bromo-1-(4-methyl-2-(pyrazin-2-yl)thiazol-5-yl)ethan-1-one

This compound was obtained from a commercial source (Oakwood Chemical, West Columbia, South Carolina).

Procedure 2

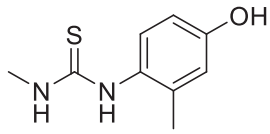

1-(4-Hydroxy-2-methylphenyl)-3-methylthiourea (7)

To a solution of 4-amino-3-methylphenol (1 g, 8.12 mmol) in THF (27.07 ml, 8.12 mmol) was added isothiocyanatomethane (610.36 μl, 8.93 mmol). The mixture was stirred at 60°C overnight then concentrated under reduced pressure. The residue was purified by flash chromatography (using a gradient of 10% ethyl acetate in hexanes to 100% ethyl acetate) to afford 1-(4-hydroxy-2-methylphenyl)-3-methylthiourea (1.05 g, 5.35 mmol, 65.9 % yield) **^{1}H NMR** (400 MHz, DMSO-d_6) δ 9.30 (s, 1H), 8.83 (s, 1H), 6.98 (d, J = 57.0 Hz, 1H),

6.84 (d, *J* = 8.4 Hz, 1H), 6.60 (d, *J* = 2.6 Hz, 1H), 6.54 (dd, *J* = 8.4, 2.7 Hz, 1H), 2.81 (d, *J* = 4.5 Hz, 3H), 2.02 (s, 3H). **ESI-MS** *m/z* 197.1 [(M + H)$^+$; calcd. for $C_9H_{13}N_2OS$: 197.08].

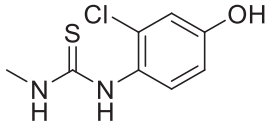

1-(2-Chloro-4-hydroxyphenyl)-3-methylthiourea (8)

To a solution of 4-amino-3-chlorophenol (0.749 g, 5.22 mmol) in THF (17.39 ml, 5.22 mmol) was added isothiocyanatomethane (427.79 μl, 6.26 mmol). The solution was stirred at 60°C overnight. The resulting suspension was cooled to room temperature and filtered. The remaining solid was washed with ethanol to produce 1-(2-chloro-4-hydroxyphenyl)-3-methylthiourea (785 mg, 3.62 mmol, 69.4 % yield) **^{1}H NMR** (400 MHz, methanol-d_4) δ 7.16 (d, *J* = 8.7 Hz, 1H), 6.88 (d, *J* = 2.7 Hz, 1H), 6.73 (dd, *J* = 8.7, 2.7 Hz, 1H), 2.97 (s, 3H). **ESI-MS** *m/z* 217.1 [(M + H)$^+$; calcd. for $C_8H_{10}ClN_2OS$: 217.02].

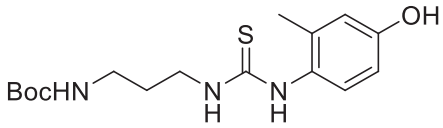

Tert-butyl (3-(3-(4-hydroxy-2-methylphenyl)thioureido)propyl)carbamate (9)

To a solution of 4-amino-3-methylphenol (50 mg, 406.00 μmol) in THF (2.0 ml, 24.41 mmol) was added tert-butyl (3-isothiocyanatopropyl)carbamate (131.73 mg, 609.00 μmol). The mixture was stirred at room temperature for 3 hours. An LC/MS indicated reaction completion. The mixture was concentrated under reduced pressure. The residue was purified by flash chromatography (using a gradient of 10% ethyl acetate in hexanes to 100% ethyl acetate) to provide tert-butyl (3-(3-(4-hydroxy-2-methylphenyl)thioureido) propyl)carbamate (117 mg, 344.67 μmol, 84.9 % yield). **^{1}H NMR** (400 MHz, acetone-d_6) δ 8.44 (br s, 1H), 8.30 (br s, 1H), 6.99 (d, *J* = 8.4 Hz, 1H), 6.83 (br s, 1H), 6.75 (d, *J* = 2.7 Hz, 1H), 6.68 (dd, *J* = 8.4, 2.8 Hz, 1H), 6.09 (br s, 1H), 3.63 (q, *J* = 6.3 Hz, 2H), 3.06 (q, *J* = 6.3 Hz, 3H), 2.17 (s, 3H), 1.74 – 1.61 (m, 2H), 1.36 (s, 9H). **ESI-MS** *m/z* 340.2 [(M + H)$^+$; calcd. for $C_{16}H_{26}N_3O_3S$: 340.17].

Procedure 3

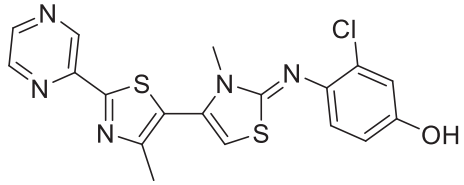

(Z)-3-chloro-4-((3,4'-dimethyl-2'-(pyrazin-2-yl)-[4,5'-bithiazol]-2(3H)-ylidene)amino)phenol (10)

A suspension of 1-(2-chloro-4-hydroxyphenyl)-3-methylthiourea (35 mg, 161.52 μmol) and 2-bromo-1-(4-methyl-2-(pyrazin-2-yl) thiazol-5-yl)ethanone (48.16 mg, 161.52 μmol) in isopropanol (2.0 mL) was stirred with microwave heating at 100°C for 1 h. The mixture was then dissolved in methanol (1.0 mL) and triethylamine (1.0 mL). The solution was concentrated under reduced pressure. The residue was purified via flash chromatography on silica gel (using a gradient of 30% to 100% of ethyl acetate in hexanes, followed by 10% methanol in dichloromethane) to give (Z)-3-chloro-4-((3,4'-dimethyl-2'-(pyrazin-2-yl)-[4,5'-bithiazol]-2(3H)-ylidene)amino) phenol (43 mg, 103.39 μmol, 64.0 % yield). **^{1}H NMR** (400 MHz, DMSO-d_6) δ 9.47 (s, 1H), 9.32 (d, *J* = 1.5 Hz, 1H), 8.78 (d, *J* = 2.5 Hz, 1H), 8.73 (dd, *J* = 2.5, 1.5 Hz, 1H), 6.93 (d, *J* = 8.6 Hz, 1H), 6.86 (d, *J* = 2.7 Hz, 1H), 6.71 (dd, *J* = 8.6, 2.7 Hz, 1H), 6.58 (s, 1H), 3.26 (s, 3H), 2.46 (s, 3H). **ESI-MS** *m/z* 416.2 [(M + H)$^+$; calcd. for $C_{18}H_{15}ClN_5OS_2$: 416.04].

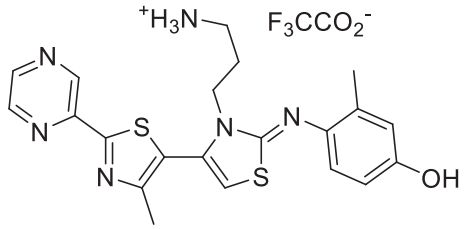

(Z)-3-(2-((4-hydroxy-2-methylphenyl)imino)-4'-methyl-2'-(pyrazin-2-yl)-[4,5'-bithiazol]-3(2H)-yl)propan-1-aminium 2,2,2-trifluoroacetate (11)

2-bromo-1-(4-methyl-2-(pyrazin-2-yl)thiazol-5-yl)ethanone (102.77 mg, 344.67 μmol) and tert-butyl (3-(3-(4-hydroxy-2-methylphenyl)thioureido)propyl)carbamate (117 mg, 344.67 μmol) were dissolved in dry isopropanol (2 mL). The solution was stirred with microwave heating at 80°C for 8 hours. Triethylamine (1.0 mL) was added. The mixture was concentrated under reduced pressure. The residue was purified by flash chromatography (using a gradient of 100% dichloromethane to 15% methanol in dichloromethane). The product was dissolved in dichloromethane (2.0 mL). TFA (1.0 mL) was added. The mixture was stirred at room temperature for 2 h. LC-MS indicated reaction completion. The mixture was concentrated under reduced pressure. The residue was dissolved in DMSO and purified by preparative HPLC to afford (Z)-4-((3-(3-aminopropyl)-4'-methyl-2'-(pyrazin-2-yl)-[4,5'-bithiazol]-2(3H)-ylidene)amino)-3-methylphenol 2,2,2-trifluoroacetate (88 mg, 112.73 μmol, 32.7 % yield) after lyophilization of the fraction containing the pure product. **^{1}H NMR** (400 MHz, DMSO-d_6) δ 9.36 (d, J = 1.5 Hz, 1H), 8.83 (d, J = 2.5 Hz, 1H), 8.77 (dd, J = 2.5, 1.5 Hz, 1H), 7.78 (br s, 3H), 7.04 (br s, 1H), 6.77 (d, J = 2.2 Hz, 1H), 6.70 (dd, J = 8.5, 2.3 Hz, 1H), 4.00 – 3.90 (m, 2H), 2.95 – 2.68 (m, 2H), 2.54 (s, 1H), 2.48 (s, 3H), 2.18 (s, 3H), 1.93 (p, J = 7.9 Hz, 2H). **ESI-MS** *m/z* 439.2 [(M + H)$^+$; calcd. for $C_{21}H_{23}N_6OS_2$: 439.14

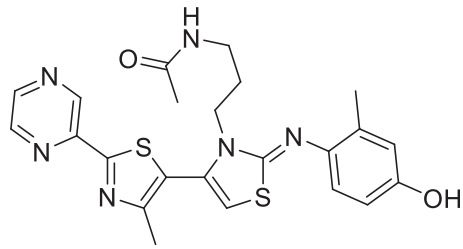

(Z)-N-(3-(2-((4-hydroxy-2-methylphenyl)imino)-4'-methyl-2'-(pyrazin-2-yl)-[4,5'-bithiazol]-3(2H)-yl)propyl) acetamide (12)

Acetic anhydride (1.90 μl, 20.18 μmol was added dropwise to a solution of (Z)-4-((3-(3-aminopropyl)-4'-methyl-2'-(pyrazin-2-yl)-[4,5'-bithiazol]-2(3H)-ylidene)amino)-3-methylphenol 2,2,2-trifluoroacetate (15 mg, 19.22 μmol) in pyridine (64.05 μl, 19.22 μmol)). The mixture was stirred at room temperature for 30 minutes. An LC/MS indicated reaction completion. The reaction mixture was concentrated under reduced pressure. The residue was purified using flash chromatography (with a gradient of 30% to 100% ethyl acetate in hexanes) to provide (Z)-N-(3-(2-((4-hydroxy-2-methylphenyl)imino)-4'-methyl-2'-(pyrazin-2-yl)-[4,5'-bithiazol]-3(2H)-yl)propyl)acetamide (4.73 mg, 9.84 μmol, 51.2 % yield). **^{1}H NMR** (400 MHz, methanol-d_4) δ 9.37 (d, J = 1.4 Hz, 1H), 8.68 (d, J = 2.5 Hz, 1H), 8.66 (dd, J = 2.5, 1.5 Hz, 1H), 6.83 (d, J = 8.4 Hz, 1H), 6.73 (d, J = 2.7 Hz, 1H), 6.65 (dd, J = 8.4, 2.8 Hz, 1H), 6.43 (s, 1H), 3.95 – 3.81 (m, 2H), 3.14 (t, J = 6.5 Hz, 2H), 2.66 (s, 1H), 2.50 (s, 3H), 2.16 (s, 3H), 1.90 (p, J = 6.8 Hz, 2H), 1.75 (s, 3H). **ESI-MS** *m/z* 481.2 [(M + H)$^+$; calcd. for $C_{23}H_{25}N_6O_2S_2$: 481.15].

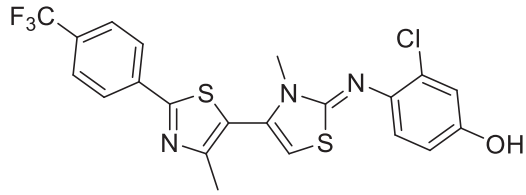

(Z)-3-chloro-4-((3,4'-dimethyl-2'-(4-(trifluoromethyl)phenyl)-[4,5'-bithiazol]-2(3H)-ylidene)amino)phenol (13)

This compound was synthesized as previously described for (Z)-3-chloro-4-((3,4'-dimethyl-2'-(pyrazin-2-yl)-[4,5'-bithiazol]-2(3H)-ylidene)amino)phenol. **^{1}H NMR** (400 MHz, DMSO-d_6) δ 9.93 (br s, 1H), 8.15 (d, J = 8.1 Hz, 2H), 7.87 (d, J = 8.2 Hz, 2H), 7.13 (d, J = 8.5 Hz, 1H), 6.94 (d, J = 2.7 Hz, 1H), 6.89 (br s, 1H), 6.79 (dd, J = 8.6, 2.7 Hz, 1H), 3.37 (s, 3H), 2.42 (s, 3H). **ESI-MS** *m/z* 482.0 [(M + H)$^+$; calcd. for $C_{21}H_{16}ClF_3N_3OS_2$: 482.04].

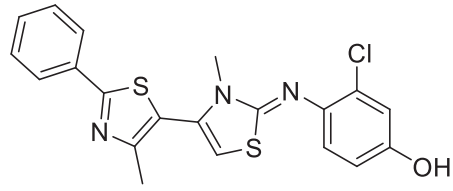

(Z)-3-chloro-4-((3,4'-dimethyl-2'-phenyl-[4,5'-bithiazol]-2(3H)-ylidene)amino)phenol (14)

This compound was synthesized as previously described for (Z)-3-chloro-4-((3,4'-dimethyl-2'-(pyrazin-2-yl)-[4,5'-bithiazol]-2(3H)-ylidene)amino)phenol. **^{1}H NMR** (400 MHz, DMSO-d_6) δ 7.97 (dd, J = 6.5, 3.1 Hz, 2H), 7.64 – 7.47 (m, 3H), 7.22 (s, 1H), 6.99 (d, J = 2.5 Hz, 1H), 6.84 (dd, J = 8.5, 2.7 Hz, 1H), 3.42 (s, 3H), 2.43 (s, 3H). **ESI-MS** *m/z* 414.0 [(M + H)$^+$; calcd. for $C_{20}H_{17}ClN_3OS_2$: 414.05].

Procedure 4

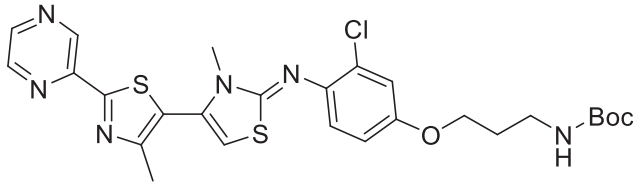

(Z)-tert-butyl (3-(3-chloro-4-((3,4'-dimethyl-2'-(pyrazin-2-yl)-[4,5'-bithiazol]-2(3H)-ylidene)amino)phenoxy)propyl) carbamate (15)

To a solution of (Z)-3-chloro-4-((3,4'-dimethyl-2'-(pyrazin-2-yl)-[4,5'-bithiazol]-2(3H)-ylidene)amino)phenol (50 mg, 120.22 μmol) in THF (0.4 mL) was added triphenylphosphine (63.06 mg, 240.43 μmol) and tert-butyl (3-hydroxypropyl)carbamate (41.10 μl, 240.43 μmol). (E)-diisopropyl diazene-1,2-dicarboxylate (47.34 μl, 240.43 μmol) was then added dropwise. The reaction mixture was stirred at room temperature for 3 h. Upon reaction completion, the mixture was purified by preparative HPLC, using a gradient of 10% acetonitrile in water (containing 0.1% trifluoroacetic acid) to 100% in acetonitrile (containing 0.1% trifluoroacetic acid), to give (Z)-tert-butyl (3-(3-chloro-4-((3,4'-dimethyl-2'-(pyrazin-2-yl)-[4,5'-bithiazol]-2(3H)-ylidene)amino)phenoxy)propyl)carbamate (43 mg, 75.03 μmol, 62.4 % yield). **^{1}H NMR. ESI-MS** *m/z* 573.4 [(M + H)$^+$; calcd. for $C_{26}H_{30}ClN_6O_3S_2$: 573.15].

Procedure 5

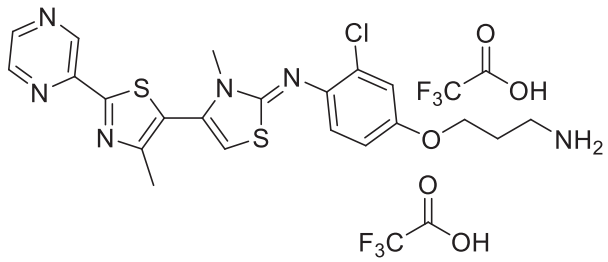

(Z)-3-(3-chloro-4-((3,4'-dimethyl-2'-(pyrazin-2-yl)-[4,5'-bithiazol]-2(3H)-ylidene)amino)phenoxy)propan-1-amine bis(2,2,2-trifluoroacetate) (16)

To a solution of (Z)-tert-butyl (3-(3-chloro-4-((3,4'-dimethyl-2'-(pyrazin-2-yl)-[4,5'-bithiazol]-2(3H)-ylidene)amino)phenoxy)propyl) carbamate (43 mg, 75.03 μmol) in dichloromethane (2 mL) was added trifluoroacetic acid (2 mL). The mixture was stirred at room temperature for 30 minutes. LC/MS indicated reaction completion. The solvents were removed under reduced pressure to afford (Z)-3-(3-chloro-4-((3,4'-dimethyl-2'-(pyrazin-2-yl)-[4,5'-bithiazol]-2(3H)-ylidene)amino)phenoxy)propan-1-amine bis(2,2,2-trifluoroacetate) (49 mg, 69.89 μmol, 93.2 % yield). **^{1}H NMR. ESI-MS** *m/z* 473.3 [(M + H)$^+$; calcd. for $C_{21}H_{22}ClN_6OS_2$: 473.10].

Procedure 6

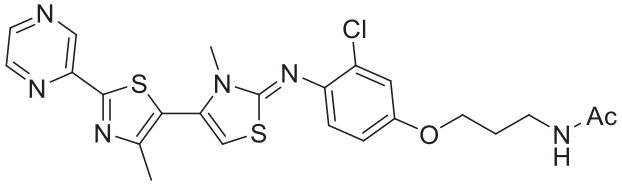

(Z)-N-(3-(3-chloro-4-((3,4'-dimethyl-2'-(pyrazin-2-yl)-[4,5'-bithiazol]-2(3H)-ylidene)amino)phenoxy)propyl) acetamide (17)

(Z)-3-chloro-4-((3,4'-dimethyl-2'-(pyrazin-2-yl)-[4,5'-bithiazol]-2(3H)-ylidene)amino)phenol (5.8 mg, 13.95 μmol), tert-butyl (4-hydroxypropyl)carbamate (5.28 mg, 30.13 μmol), and triphenylphosphine (7.32 mg, 27.89 μmol) were dissolved in THF (46.48 μl, 13.95 μmol). (E)-diisopropyl diazene-1,2-dicarboxylate (5.49 μl, 27.89 μmol) was added dropwise at 0°C. The mixture was stirred at room temperature for 2 h. LC/MS indicated reaction completion. The reaction mixture was concentrated under reduced pressure. The residue was dissolved in dichloromethane (1.0 mL). TFA was added (1.0 mL) and the mixture was stirred for 30 minutes. LC/MS indicated full deprotection. The mixture was concentrated under reduced pressure. The residue was dissolved in pyridine (1.0 mL). Acetic anhydride (7 μl, 74.19 μmol) was added. The reaction mixture was stirred at room temperature for 20 min and concentrated under reduced pressure. The residue was purified using preparative HPLC, with a gradient of 10% acetonitrile in water (containing

0.1% trifluoroacetic acid) to 100% in acetonitrile (containing 0.1% trifluoroacetic acid), to give (Z)-N-(3-(3-chloro-4-((3,4'-dimethyl-2'-(pyrazin-2-yl)-[4,5'-bithiazol]-2(3H)-ylidene)amino)phenoxy)propyl)acetamide 2,2,2-trifluoroacetate (5.23 mg, 8.31 μmol, 59.6 % yield). **^{1}H NMR** (400 MHz, DMSO-d_6) δ 9.33 (d, *J* = 1.5 Hz, 1H), 8.79 (d, *J* = 2.5 Hz, 1H), 8.74 (dd, *J* = 2.5, 1.5 Hz, 1H), 7.89 (br t, *J* = 5.4 Hz, 1H), 7.17 (br d, *J* = 8.7 Hz, 1H), 7.12 (d, *J* = 2.8 Hz, 1H), 6.94 (dd, *J* = 8.8, 2.8 Hz, 1H), 6.79 (br s, 1H), 3.99 (t, *J* = 6.3 Hz, 2H), 3.34 (s, 3H), 3.17 (q, *J* = 6.8 Hz, 2H), 2.46 (s, 3H), 1.88 – 1.73 (m, 5H). **ESI-MS** *m/z* 515.3 [(M + H)$^+$; calcd. for $C_{23}H_{24}ClN_6O_2S_2$: 515.11].

Procedure 7

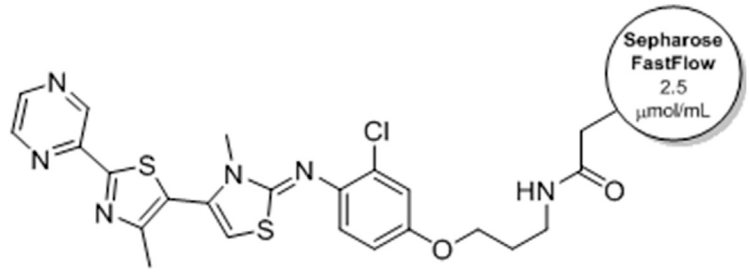

Loading of Thiazolimine onto Sepharose FastFlow Beads (18)

Sepharose beads (8 mL of a 1:1 suspension in isopropanol) were separated in two 15 mL conical tubes (Falcon) and centrifuged at 1200 rpm for 2 minutes. The supernatant was removed. DMSO (10 mL) was added to each tube. The beads were resuspended and the tubes were centrifuged as previously described. This centrifugation and re-suspension process was repeated twice, then once more with the exception that anhydrous DMSO was used to suspend the beads. The supernatant and excess beads were removed to adjust the volume to 2 mL of beads in each tube. Anhydrous DMSO (2.0 mL) was added to each tube, followed by a 50 mM DMSO solution of (Z)-4-(3-aminopropoxy)-2-chloro-N-(3,4'-dimethyl-2'-(pyrazin-2-yl)-[4,5'-bithiazol]-2(3H)-ylidene)aniline 2,2,2-trifluoroacetate (a total of 200.00 μl, 10 μmol). Triethylamine (60 μl, 430.48 μmol) was added to each tube and the beads were resuspended. The suspension was centrifuged at 1200 rpm for 2 minutes. An aliquot (20 μL) of the supernatant in each tube was diluted 1:1 with DMSO. The samples were analyzed using LC-MS to quantify the initial amount free amine in the reaction.

The beads were stirred at room temperature via inversion overnight (16 h) then centrifuged. An LC/MS of the aliquot of the supernatants no longer showed the presence of free amine. Ethanolamine (200 μl, 3.31 μmol) was then added to each tube. The mixture was stirred at room temperature overnight. The beads were centrifuged. The supernatant was removed, and the beads were resuspended in anhydrous DMSO (10 mL) and centrifuged. The supernatant was removed and the beads were washed three times with anhydrous ethanol (10 mL portions). The recovered beads from both tubes were combined and suspended in anhydrous ethanol in a 1:1 ratio.

QUANTIFICATION AND STATISTICAL ANALYSIS

Statisitical details can be found in the STAR Methods sub-section for each experiment, or in the Results section. Uncertainties are expressed as the standard error in the mean. For *in vitro* experiments, *n* represents the number of independent biological replicates; for *in vivo* experiments, *n* represents the number of animals. For correlations of potencies in biochemical/cell-based experiments, Spearman's rank order correlation was used, with use of the *t*-test for calculation of p values (reported in the Results section).